The Astrophysical Journal, 849:111 (15pp), 2017 November 10 https://doi.org/10.3847/1538-4357/aa911d

The AGN–Star Formation Connection: Future Prospects with *JWST*

Allison Kirkpatrick[1], Stacey Alberts[2], Alexandra Pope[3], Guillermo Barro[4], Matteo Bonato[5], Dale D. Kocevski[6], Pablo Pérez-González[7], George H. Rieke[2], Lucia Rodríguez-Muñoz[8], Anna Sajina[9], Norman A. Grogin[10], Kameswara Bharadwaj Mantha[11], Viraj Pandya[12], Janine Pforr[13], Mara Salvato[14], and Paola Santini[15]
[1] Yale Center for Astronomy & Astrophysics, Physics Department, P.O. Box 208120, New Haven, CT 06520, USA; allison.kirkpatrick@yale.edu
[2] Steward Observatory, University of Arizona, 933 North Cherry Avenue, Tucson, AZ 85721, USA
[3] Department of Astronomy, University of Massachusetts, Amherst, MA 01002, USA
[4] University of California, 501 Campbell Hall, Berkeley, CA 94720 Santa Cruz, USA
[5] INAF—Osservatorio di Radioastronomia, Via Piero Gobetti 101, I-40129 Bologna, Italy
[6] Department of Physics and Astronomy, Colby College, Waterville, ME 04901, USA
[7] Departamento de Astrofísica y CC. de la Atmósfera, Universidad Complutense de Madrid, E-28040 Madrid, Spain
[8] Dipartimento di Fisica e Astronomia, Università di Padova, vicolo dellOsservatorio 2, I-35122 Padova, Italy
[9] Department of Physics & Astronomy, Tufts University, Medford, MA 02155, USA
[10] Space Telescope Science Institute, 3700 San Martin Drive, Baltimore, MD 21218, USA
[11] Department of Physics and Astronomy, University of Missouri–Kansas City, 5110 Rockhill Road, Kansas City, MO 64110, USA
[12] UCO/Lick Observatory, Department of Astronomy and Astrophysics, University of California, Santa Cruz, CA 95064, USA
[13] ESA/ESTEC, Keplerlaan 1, 2201 AZ Noordwijk, The Netherlands
[14] Max Planck Institut für Extraterrestrische Physik, Giessenbachstraße, D-85748 Garching, Germany
[15] INAF—Osservatorio Astronomico di Roma, via di Frascati 33, I-00078 Monte Porzio Catone, Italy
Received 2017 June 26; revised 2017 September 14; accepted 2017 September 28; published 2017 November 7

Abstract

The bulk of the stellar growth over cosmic time is dominated by IR-luminous galaxies at cosmic noon ($z = 1$–2), many of which harbor a hidden active galactic nucleus (AGN). We use state-of-the-art infrared color diagnostics, combining *Spitzer* and *Herschel* observations, to separate dust-obscured AGNs from dusty star-forming galaxies (SFGs) in the CANDELS and COSMOS surveys. We calculate 24 μm counts of SFGs, AGN/star-forming "Composites," and AGNs. AGNs and Composites dominate the counts above 0.8 mJy at 24 μm, and Composites form at least 25% of an IR sample even to faint detection limits. We develop methods to use the Mid-Infrared Instrument (MIRI) on *JWST* to identify dust-obscured AGNs and Composite galaxies from $z \sim 1$–2. With the sensitivity and spacing of MIRI filters, we will detect >4 times as many AGN hosts as with *Spitzer*/IRAC criteria. Any star formation rates based on the 7.7 μm PAH feature (likely to be applied to MIRI photometry) must be corrected for the contribution of the AGN, or the star formation rate will be overestimated by ∼35% for cases where the AGN provides half the IR luminosity and ∼50% when the AGN accounts for 90% of the luminosity. Finally, we demonstrate that our MIRI color technique can select AGNs with an Eddington ratio of $\lambda_{\rm Edd} \sim 0.01$ and will identify AGN hosts with a higher specific star formation rate than X-ray techniques alone. *JWST*/MIRI will enable critical steps forward in identifying and understanding dust-obscured AGNs and the link to their host galaxies.

Key words: galaxies: active – galaxies: photometry – galaxies: star formation

1. Introduction

The galaxies most actively contributing to the buildup of stellar mass at cosmic noon ($z \sim 1$–2) contain large amounts of dust (e.g., Murphy et al. 2011; Madau & Dickinson 2014, and references therein). This dust obscures the majority of star formation, making it necessary to study these galaxies through their dust emission at infrared wavelengths (Madau & Dickinson 2014). Additionally, the majority of supermassive black hole growth at these redshifts is also heavily dust obscured (e.g., Hickox & Markevitch 2007). Many of the massive dusty galaxies contain a true mix of star formation and obscured black hole growth, the obscured signatures of which can be seen in their infrared spectral energy distribution (SED). These galaxies are then ideal laboratories for understanding the physical link between star formation and active galactic nuclei (AGNs). The AGN–star formation connection is an open question, particularly whether AGN feedback is a key component of star formation quenching, and whether all galaxies have a distinct star formation phase followed by an AGN phase before ultimately quenching (e.g., Sanders et al. 1998; Hopkins et al. 2006). The nature of AGNs within strongly star-forming galaxies (SFGs) (what we term "Composites") is even more uncertain. Do these objects represent a unique phase between SFGs and AGNs? Unfortunately, due to limitations of previous space telescopes, detailed studies of the energetics of these objects were severely restricted, but the *James Webb Space Telescope* (*JWST*) will reveal their true nature.

Prior to *JWST*, the most reliable method for identifying Composites and disentangling AGN emission from star formation was with mid-IR spectroscopy, particularly from the IRS instrument on board the *Spitzer Space Telescope*. The low-resolution spectra can be modeled as a combination of star formation features (most notably the polycyclic aromatic hydrocarbons [PAHs] that exist in photodissociation regions and in stellar/H II regions) and hot continuum emission primarily arising from a dusty torus surrounding the accreting black hole (Pope et al. 2008; Coppin et al. 2010; Kirkpatrick et al. 2012; Sajina & Yan et al. 2012; Hernán-Caballero et al. 2015; Kirkpatrick et al. 2015). In this way, the division of IR luminosity between star formation and an AGN can be quantified. The medium-resolution spectrometer (Wells

et al. 2015), which is part of the Mid-Infrared Instrument (MIRI) on *JWST*, will enable separation of PAH emission from continuum in the same manner, but with higher resolution and on smaller spatial scales within host galaxies. It will also enable detection of high-ionization gas lines excited by the AGN (Bonato et al. 2017), further improving our ability to detect and measure the physical properties (such as accretion rates and Eddington ratios) of dust-obscured black holes.

As there are only a few hundred *Spitzer* IRS spectra available for distant galaxies (Kirkpatrick et al. 2015), color techniques were also developed to identify large samples of luminous dust-obscured AGNs. The most popular color selection techniques are with *Spitzer* IRAC photometry (Lacy et al. 2004; Stern et al. 2005; Alonso-Herrero et al. 2006; Donley et al. 2012), which separates AGNs using different combinations of the 3.6, 4.5, 5.8, and 8.0 μm filters. The original techniques presented in Lacy et al. (2004) and Stern et al. (2005) were limited to the most luminous AGNs and become increasingly contaminated with galaxies when deeper IR data are used (Mendez et al. 2013). Moreover, with increasing redshift, the rest wavelengths of these bands decrease, causing contamination of the AGN signatures by SFGs to become significant such that the original IRAC-based criteria cannot be applied. Donley et al. (2012) propose more conservative IRAC criteria that, at cosmic noon, essentially separate galaxies that exhibit a so-called stellar bump (emission from stars that peaks at $\sim$1.6 μm and then declines to a minimum around $\sim$5 μm) from those that do not, where the torus radiation is strong enough to fill in the dip in the star-forming spectrum around 3–5 μm, producing power-law emission such as is typical of unobscured AGNs (e.g., Elvis et al. 1994). The Donley et al. (2012) criteria increase the reliability of AGN color selection, although they are less complete owing to excluding Composites, where the IR emission of the AGN does not dominate over the star formation.

For the purposes of probing the AGN–star formation connection, the limitation of IRAC techniques is that AGNs within strongly SFGs can have different levels of host contamination. Then, many galaxies containing AGN signatures at longer wavelengths will also include a stellar bump and therefore be missed (Kirkpatrick et al. 2013, 2015). To alleviate host contamination, Messias et al. (2012) propose combining *K* band with IRAC and 24 μm to separate AGNs from host galaxies all the way out to $z \sim 7$. Going further, including mid-IR *and* far-IR (FIR) colors can greatly improve the selection of Composite galaxies, since this will trace the contribution of warmer AGN-heated dust compared with cold dust from the diffuse interstellar medium in the host galaxy (Kirkpatrick et al. 2015). However, this requires observations from the *Herschel Space Observatory*, which have a large beam size and do not reach the same depths as *Spitzer* observations. Perhaps the most reliable method is fitting a full suite of photometry from the UV to the FIR. This is an emergent technique that can also be used to quantify the fraction of bolometric luminosity due to an AGN (e.g., Calistro Rivera et al. 2016). MIRI photometry can be combined with NIRcam and *Hubble Space Telescope* photometry to simultaneously quantify the stellar population, dust obscuration, and AGN energetics. The drawback to this technique is that it requires a careful merger of photometry from different instruments and measured in different ways. It also is more sensitive to degeneracy in the solution and assumes a good understanding of the templates used in the fit.

MIRI will greatly improve color selection techniques owing to the increased sensitivity and the number of transmission filters covering the mid-infrared (Bouchet et al. 2015; Glasse et al. 2015). Now, we will be able to separate AGNs from SFGs by comparing PAH emission with the minimum emission from stars that occurs around 5 μm; in AGNs, the stellar minimum is not visible owing to strong torus emission, and Composites will lie in between strong AGNs and pure SFGs in color space.

In this paper, we build on the *Herschel* and *Spitzer* color selection techniques initially presented in Kirkpatrick et al. (2013) to identify Composite galaxies at $z \sim 1$–2 using the CANDELS (0.24 deg^2) and the entire COSMOS (2 deg^2) fields. We present galaxy counts of 24 μm sources classified as SFGs, AGNs, or Composites based on their IR colors, making this the first identified statistical sample of Composites at cosmic noon. We use this sample to predict black hole and star formation properties of samples that *JWST*/MIRI will identify. We also present color diagnostics for identifying both AGNs and Composites using *JWST*/MIRI filters in three redshift bins. Throughout this paper, we assume a standard cosmology with $H_0 = 70$ km s^{-1} Mpc^{-1}, $\Omega_M = 0.3$, and $\Omega_\Lambda = 0.7$.

2. CANDELS and COSMOS Catalogs

To calculate galaxy counts, we use *Spitzer* and *Herschel* photometry from the COSMOS, EGS, GOODS-S, and UDS fields from the Cosmic Assembly Near-IR Deep Extragalactic Survey (CANDELS, P.I. S. Faber and H. Ferguson; GOODS-*Herschel*, P.I. D. Elbaz; CANDELS-*Herschel*, P.I. M. Dickinson). We do not include GOODS-N, as, at the time of the writing of this paper, the IR catalog does not have uniquely identified optical counterparts. We also use photometric redshifts ($z_{\rm phot}$; Dahlen et al. 2013; Stefanon et al. 2017) and M_* (Santini et al. 2015; Stefanon et al. 2017). The stellar masses are derived by fitting the CANDELS UV/Optical photometry in 10 different ways, each fit using a different code, priors, grid sampling, and star formation histories (SFHs). The final M_* is the median from the different fits, and it is stable against the choice of SFH and the range of metallicity, extinction, and age parameter grid sampling. The CANDELS $z_{\rm phot}$s are the median redshift determined through five separate codes that fit templates to the UV/optical/near-IR data (the technique is fully described in Dahlen et al. 2013). Comparison of $z_{\rm phot}$s with spectroscopic redshifts for a limited sample gives $\sigma = 0.03$, where σ is the rms of $(z_{\rm phot} - z_{\rm spec})/(1 + z_{\rm spec})$. As we sort sources into redshift bins of $\Delta z = 0.5$, we do not expect the uncertainty on the photometric redshifts to be a dominant source of uncertainty in our results. We will be using the $z_{\rm phot}$s to help classify sources as AGNs, SFGs, or Composites.

MIPS 24 μm and *Herschel* PACS and SPIRE catalogs were built following the prior-based point-spread function (PSF) fitting method described in Pérez-González et al. (2005, MIPS photometry) and Pérez-González et al. (2010, merged MIPS plus *Herschel* photometry). For additional details on the methods used for *Herschel* catalog building, see Rawle et al. (2016). Briefly, the algorithm uses IRAC and MIPS data to extract photometry for sources in longer-wavelength data using positional priors. Deblending is not possible when sources lie closer than 75% of the FWHM of the PSF in each band, making this value a minimum separation required to perform

deblending. The final product of the cataloging method is a list of IRAC sources with possible counterparts in all longer-wavelength data. In this sense, several IRAC sources might be identified with the same MIPS or *Herschel* source. This is what we call multiplicity. The multiplicity for MIPS and PACS is in more than 95% of the cases equal to 1 (i.e., only one IRAC source is identified with a single MIPS and PACS source), but it is higher for SPIRE (on average, six IRAC sources are found within the FWHM of the SPIRE 250 μm PSF). In order to identify the "right" IRAC counterpart for each FIR source, we follow the method described in L. Rodríguez-Muñóz et al. (2017, in preparation). In practice, we choose the MIPS most probable counterpart as the brightest IRAC candidate. Then, we shift this methodology to longer-wavelength bands. We identify the most likely PACS counterpart as the brightest source in MIPS 24 μm among the different candidates. When MIPS is not available, we use the reddest IRAC band in which the source is detected. We note that using IRAC as a tracer of PACS emitters can lead to spurious identifications. For this reason, these cases are flagged to evaluate the possible impact in the results. Finally, we use the fluxes in PACS or MIPS (if PACS is not available) to find the counterparts of the SPIRE sources. The flux of each FIR source is assigned to a single IRAC counterpart. The FWHM of the PACS PSF is roughly the same as for MIPS, so the most serious concern in this work is matching to the SPIRE 250 μm sources. We are primarily using the IR photometric catalogs to calculate galaxy counts. As a check, we remove all classifications of galaxies (as SFGs, AGNs, and Composites) that were done with SPIRE data (described in the following section). Our main result, the galaxy counts at cosmic noon, are unchanged, giving confidence that any misidentification of a SPIRE source with an MIPS and IRAC counterpart is not biasing our results.

We have also added sources from the COSMOS survey (Scoville 2007), which are necessary to boost the bright end of the galaxy counts, due to the small survey area of CANDELS (0.22 deg^2). We use the public COSMOS2015 catalog in Laigle et al. (2016), which presents multiwavelength data, as well as stellar masses and photometric redshifts. The *Spitzer* IRAC data in this catalog originally come from SPLASH COSMOS and S-COSMOS (Sanders et al. 2007), while the MIPS 24 μm observations are described in Le Floc'h et al. (2009). The catalog also contains *Herschel* observations from the PEP guaranteed time program (Lutz et al. 2011) and the HERMES consortium (Oliver et al. 2012). The counterpart identification and procedures for measuring stellar masses and photometric redshifts are fully described in Laigle et al. (2016).

The difficulty in matching MIPS, PACS, and SPIRE sources with their IRAC counterparts underscores the improvements that will be made by using MIRI color selection to identify AGN host galaxies, since the much smaller PSF ($<1''$ for all filters) and smaller spectral range used will obviate the need for counterpart identification for robust color diagnostics.

3. IR Identification of AGNs and Composites

To identify SFGs, composites, and AGNs, we build on the color techniques in Kirkpatrick et al. (2013, 2015) that sample the full IR SED. At $z \sim 1$–2, the color $S_8/S_{3.6}$ separates sources with a strong stellar bump, present in SFGs, from those with hot torus emission, found in AGNs. Composites span a range in this color, depending on the ratio of relative strengths of the AGN and host galaxy emission and the amount of obscuration of the AGN due to dust.[16] S_{100} and S_{250} trace the peak of the IR SED, which is generally dominated by the cold dust in the diffuse interstellar medium (ISM). S_{24} traces the PAH emission in SFGs or the warm dust emission heated by the AGN. Then, the color S_{250}/S_{24} or S_{100}/S_{24} will measure the relative amounts of cold emission to warm dust or PAH emission, and this ratio is markedly higher in SFGs. However, significant scatter is introduced into color selection by redshift, since S_{24} will move over different PAH features and silicate absorption at 9.7 μm, changing where SFGs lie in color space. We can more robustly identify SFGs, AGNs, and Composites if we introduce a redshift criterion.

The color diagnostics (S_{250}/S_{24} versus $S_8/S_{3.6}$ and S_{100}/S_{24} versus $S_8/S_{3.6}$) were calibrated with a sample of 343 galaxies with *Spitzer* IRS spectroscopy and $S_{24} > 0.1$ mJy spanning the range $z \sim 0.5$–4 and $M_* > 10^{10}\,M_\odot$. This sample is fully described in Kirkpatrick et al. (2012, 2015) and Sajina & Yan et al. (2012). We identified SFGs, Composites, and AGNs through spectral decomposition, where we fit the mid-IR spectrum (5–18 μm rest frame) with a model consisting of PAH features for star formation, a power-law continuum for the AGN, and extinction. We then quantified the AGN emission, $f(\mathrm{AGN})_{\mathrm{MIR}}$, as the fraction of mid-IR luminosity (5–15 μm) due to the power-law continuum. We define three classes of galaxies based on $f(\mathrm{AGN})_{\mathrm{MIR}}$, and we also report the fraction of MIR luminosity solely due to emission from the PAH features in the 5–15 μm range: (1) SFGs are dominated by PAH emission ($f(\mathrm{AGN})_{\mathrm{MIR}} < 0.2$, $L_{\mathrm{PAH}}/L_{\mathrm{MIR}} > 0.6$); (2) AGNs have negligible PAH emission ($f(\mathrm{AGN})_{\mathrm{MIR}} > 0.8$, $L_{\mathrm{PAH}}/L_{\mathrm{MIR}} < 0.15$); (3) Composites have a mix of PAH and continuum emission ($f(\mathrm{AGN})_{\mathrm{MIR}} = 0.2$–$0.8$, $L_{\mathrm{PAH}}/L_{\mathrm{MIR}} = 0.15$–$0.6$). We note that below we will redefine these thresholds for color selection. We relate the mid-IR classification to the full IR SED by creating empirical templates using data from *Spitzer* and *Herschel*. We sort sources into subsamples based on $f(\mathrm{AGN})_{\mathrm{MIR}}$ and, after normalization, determine the median L_ν in differential bin sizes of λ (Kirkpatrick et al. 2012, 2015). The Kirkpatrick et al. (2015) SEDs are the first comprehensive public library of IR templates specifically designed for high-redshift galaxies that account for AGN emission.

We create a redshift-dependent color diagnostic through use of the empirical MIR-based template library from Kirkpatrick et al. (2015). We use a template library because our spectroscopic sample of 343 sources is not large enough to separate sources into multiple z bins. The MIR-based library contains 11 templates created from our spectroscopic sources that demonstrate the change in IR spectral shape as the contribution of the AGN to the mid-IR luminosity increases, in steps of $\Delta f(\mathrm{AGN})_{\mathrm{MIR}} = 0.1$. There are many AGN and SFG templates in the literature. However, due to the exceptional multi-wavelength data and large sample size, the Kirkpatrick et al. (2015) library is the most robust empirical set of templates at cosmic noon for dusty galaxies. In the 1–20 μm (rest wavelength) range critical for most of our color sorting the AGN templates agree well (Lyu & Rieke 2017). At wavelengths longer than 20 μm, there is considerable

[16] In fact, heavily obscured AGNs such as NGC 1068, the Circinus galaxy, and IRAS 08572+3915 have SEDs that drop rapidly from 10 μm toward shorter wavelengths and will show the near-IR stellar spectral peak characteristic of SFGs. Hereafter, we refer to "AGNs" with the understanding that the samples discussed may suffer from incompleteness of sources like these. This issue is discussed further in Section 4.1.

divergence; fortunately for our goals, the star-forming output is so dominant by 100 and 250 μm that the range of possibilities for AGN output has little effect on our results. As for SFGs, at solar metallicity, the PAH features are remarkably uniform (Spoon et al. 2007; Petric et al. 2011; Battisti et al. 2015; Shipley et al. 2016). This template library does not show a large variation in silicate absorption, which can cause us to miss some heavily obscured sources at $z \sim 1.5$, where the 9.7 μm absorption feature falls into the 24 μm band. However, this will not be a concern in the following section when we discuss MIRI color selection, as we stay blueward of this feature.

We randomly redshift each template 500 times, uniformly sampling a redshift distribution in the range $z = 0.75$–2.25. We convolve each redshifted template with the observed frame IRAC, MIPS, PACS, and SPIRE transmission filters to create photometry, and then we resample the photometry within the template uncertainties at that particular wavelength, following a Gaussian distribution. We now have a catalog of 5500 synthetic galaxies, where we know the intrinsic AGN contribution, that represent the scatter in color space of real galaxies.

Next, we create color diagrams in redshift bins of $z = 0.75$–1.25, $z = 1.25$–1.75, and $z = 1.75$–2.25. Beyond this redshift, it becomes too difficult to reliably separate Composites from SFGs with these colors. Because only a fraction of CANDELS and COSMOS sources have a SPIRE or PACS detection, we also create a color diagnostic using the colors S_{24}/S_8 versus $S_8/S_{3.6}$, although this is slightly less accurate. In each redshift bin, we divide the color space into regions of 0.2 × 0.2 dex and calculate the average $f(\mathrm{AGN})_{\mathrm{MIR}}$ and standard deviation, σ_{AGN}, of all the synthetic galaxies that lie in that region. In the Appendix, we show our three diagnostics: S_{250}/S_{24} versus $S_8/S_{3.6}$ (used when a galaxy has the appropriate photometry, as it is the most complete at selecting Composite galaxies), S_{100}/S_{24} versus $S_8/S_{3.6}$ (used when a galaxy does not have a 250 μm detection), and S_{24}/S_8 versus $S_8/S_{3.6}$ (used for all galaxies without a longer-wavelength detection).

Our color diagnostics assign sources an $f(\mathrm{AGN})_{\mathrm{MIR}}$ in bins of $\Delta f(\mathrm{AGN})_{\mathrm{MIR}} = 0.1$, but the σ_{AGN} of each region is often larger than this (see the Appendix for a visual representation). Therefore, it is more accurate to broadly group sources as SFGs, Composites, and AGNs. We determine how to group sources by comparing the $f(\mathrm{AGN})_{\mathrm{MIR}}$ assigned to each synthetic galaxy by the three different color diagnostics. There is a one-to-one correlation between $f(\mathrm{AGN})_{\mathrm{MIR}}$ (250 μm), $f(\mathrm{AGN})_{\mathrm{MIR}}$(100 μm), and $f(\mathrm{AGN})_{\mathrm{MIR}}$(24 μm), with a scatter of $\sigma = 0.15$. Accordingly, we classify as SFGs sources with $f(\mathrm{AGN})_{\mathrm{MIR}} < 0.30$, while the AGNs have $f(\mathrm{AGN})_{\mathrm{MIR}} > 0.70$ and Composites are everything in between.

We assess the completeness and reliability of our color technique by determining how many of our synthetic galaxies are correctly identified as SFGs, Composites, and AGNs in each diagnostic, and we list the completeness and reliability in Table 1. In the following definitions, we use N_{input} to represent the total number of intrinsic objects (so $N_{\mathrm{AGN,input}}$ is the number of synthetic galaxies that are intrinsically AGNs) and n_{sel} to represent the number of objects recovered by our color criteria (so $n_{\mathrm{AGN,sel}}$ is the number of intrinsic AGNs that our color selection identifies as AGNs). Completeness is defined as the fraction of AGNs (for example) selected: $n_{\mathrm{AGN,sel}}/N_{\mathrm{AGN,input}}$. Reliability is the fraction of all the sources selected by the diagnostic as AGNs (for example) that actually are, intrinsically, AGNs: $n_{\mathrm{AGN,sel}}/n_{\mathrm{all,sel}}$. The lower completeness and reliability of the Composites and SFGs are due to these sources being more easily confused with each other when relying on the limited SED coverage (particularly of the mid-IR) provided by 8.0, 24, 100, and 250 μm. By adding more bands, MIRI will allow for a more nuanced measurement of the strength of the PAH emission compared with continuum and stellar bump emission. It is also important to note that we are missing AGNs with extreme obscuration, whose IR colors could mimic those of SFGs. We discuss this issue more fully in Section 4.1.

Table 1
Completeness (Reliability) of Redshift-dependent Color Selection

Region	$z \sim 1$	$z \sim 1.5$	$z \sim 2$
S_{250}/S_{24} versus $S_8/S_{3.6}$			
AGN	93 (85)%	92 (89)%	97 (86)%
Composite	67 (67)%	81 (63)%	56 (66)%
SFG	66 (77)%	41 (75)%	64 (64)%
S_{100}/S_{24} versus $S_8/S_{3.6}$			
AGN	97 (89)%	94 (89)%	98 (81)%
Composite	69 (71)%	76 (64)%	42 (59)%
SFG	67 (75)%	46 (69)%	62 (57)%
S_{24}/S_8 versus $S_8/S_{3.6}$			
AGN	93 (85)%	90 (88)%	97 (83)%
Composite	69 (65)%	67 (66)%	48 (82)%
SFG	60 (77)%	61 (65)%	87 (68)%

Note. Completeness is defined as the percentage of sources of a given intrinsic classification that are also selected by the color diagnostic. Reliability (shown in parentheses) is the percentage of all sources classified in a given category where the intrinsic classification agrees.

We assign each CANDELS or COSMOS source with $z = 0.75$–2.25 an $f(\mathrm{AGN})_{\mathrm{MIR}}$ and associated uncertainty (σ_{AGN}) and then broadly group sources into SFGs, Composites, and AGNs. Overall, from CANDELS (COSMOS), 534 (6426) sources have been classified with S_{250}/S_{24} versus $S_8/S_{3.6}$, 864 (175) with S_{100}/S_{24} versus $S_8/S_{3.6}$, and 871 (5360) with S_{24}/S_8 versus $S_8/S_{3.6}$. From CANDELS, we also fit an additional 111 sources, which lie slightly beyond the regions (within 0.2 dex) in our color classification scheme, with the Kirkpatrick et al. (2015) template library to determine the classification. We were unable to classify 3% of sources because they lay outside the regions of our color classification scheme and were not well fit with our template library. This small percentage verifies that our template library is a robust choice and captures the intrinsic variation of dusty galaxies at cosmic noon.

3.1. Galaxy and AGN Counts

Now, we determine how traditional 24 μm number counts break down into the SFG, Composite, and AGN categories. We only consider sources with $S_{24} > 80$ μJy, which is the 80% completeness limit (Pérez-González et al. 2005). We measure directly the EGS, COSMOS, GOODS-S, and UDS field sizes covered by our sources. We show the total CANDELS +COSMOS 24 μm number counts as the open gray stars in

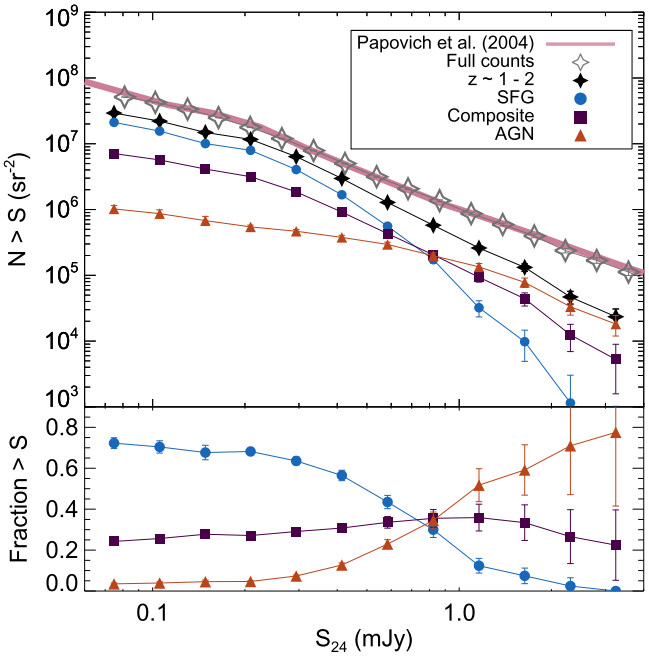

Figure 1. Top panel: cumulative 24 μm number counts for the CANDELS and COSMOS fields. The open gray stars show the number counts of all 24 μm detected sources, and these agree with the published number counts (Papovich et al. 2004; pink solid line). The filled stars show the 24 μm counts from $z = 0.75$–2.25. At the bright end, the lack of sources is due to the relatively small field sizes. We then show the contribution of SFGs ($f(\mathrm{AGN})_{\mathrm{MIR}} < 0.3$; blue circles), Composites ($0.3 \leqslant f(\mathrm{AGN})_{\mathrm{MIR}} < 0.7$; purple squares), and AGNs ($f(\mathrm{AGN})_{\mathrm{MIR}} \geqslant 0.7$; orange triangles) to the $z \sim 1$–2 number counts. Bottom panel: percentage of each subsample above a given flux threshold. At $S_{24} > 0.8$ mJy, Composites and AGNs dominate samples. Even at fainter fluxes, *JWST*/MIRI samples will contain >25% Composites.

Figure 1, and these counts are in agreement with the counts from Papovich et al. (2004). In the full COSMOS field, we take care not to double-count sources in both CANDELS and COSMOS. We plot the 24 μm counts at cosmic noon ($z = 0.75$–2.25) as the filled black stars. There is a disagreement with the full counts that arises from applying the redshift cut, and this chiefly affects the bright end ($S_{24} > 1$ mJy), which is where AGNs will dominate the counts (Kirkpatrick et al. 2013). The lack of bright sources is a result of the small field sizes of CANDELS (0.22 deg^2) and COSMOS (2 deg^2). We show how the cosmic noon counts break down into SFGs (blue), Composites (purple), and AGNs (orange). We have calculated uncertainties on the counts using a Monte Carlo technique, where we vary the $f(\mathrm{AGN})_{\mathrm{MIR}}$ for each source within its associated uncertainty and recount sources. We follow this procedure 1000 times. The counts in Figure 1 represent the mean from the Monte Carlo simulations, and the error bars are standard deviations from the Monte Carlo trials and the standard Poisson errors, summed in quadrature.

Below 0.8 mJy, SFGs dominate the counts, but AGNs become more prevalent with increasing brightness. In the bottom panel of Figure 1, we show the percentage of sources above a given flux threshold. We find that AGNs contribute ~10% at 0.3 mJy and increase to ~80% at 2 mJy, in good agreement with measurements in Brand et al. (2006) in the Boötes field. Although AGNs are frequently assumed not to be abundant in fainter IR samples, the presence of AGN hosts at $S_{24} < 100$ μJy was also seen in a small *Spitzer*/IRS spectroscopic sample of lensed galaxies at $z \sim 2$, where the authors found that 30% of the sample had IR AGN signatures and 40% had X-ray AGN signatures (Rigby et al. 2008). The Composites >25% of a sample down to the faintest flux threshold at 63% completeness, which we determined by applying the completeness estimates listed in Table 1 to the number of sources classified with each method. Then, at least 25% of a *JWST*/MIRI sample will be Composite galaxies, providing a rich data set for probing the AGN/star formation connection at cosmic noon.

4. *JWST* Color Selection

Color selection is a powerful technique for identifying likely AGNs, Composites, and SFGs. We have done an exhaustive search to identify the best MIRI filter combinations for separating galaxies into these three classes at cosmic noon by creating synthetic photometry in the *JWST*/MIRI filters from the Kirkpatrick et al. (2015) MIR-based library following the Monte Carlo technique outlined in Section 3. As many *JWST*/MIRI observations will be carried out in fields with available photometric redshifts, or in parallel with NIRcam and NIRspec observations, we include redshift information in our color diagnostics to improve reliability and completeness. We identify three diagnostics covering the ranges $z \sim 1$ ($z = 0.75$–1.25), $z \sim 1.5$ ($z = 1.25$–1.75), and $z \sim 2$ ($z = 1.75$–2.25). These three diagnostics, shown in Figure 2, are different combinations of the S_{21}, S_{18}, S_{15}, $S_{12.8}$, S_{10}, and $S_{7.7}$ filters, which cover the 6.2 and 7.7 μm PAH complexes and the 3–5 μm stellar minimum at these redshifts.

We present two methods for separating SFGs, Composites, and AGNs. First, we have determined the optimal AGN, Composite, and SFG regions, labeled in Figure 2. The boundaries of each region are circles, with AGNs lying inside the inner circle, SFGs lying outside the outer circle, and Composites lying in between.

The $z \sim 1$ boundaries are

$$\begin{aligned}\text{inner:}\ &\left(\log\frac{S_{15}}{S_{7.7}} - 0.40\right)^2 + \left(\log\frac{S_{18}}{S_{10}} - 0.38\right)^2 = 0.25^2\\ \text{outer:}\ &\left(\log\frac{S_{15}}{S_{7.7}} - 0.35\right)^2 + \left(\log\frac{S_{18}}{S_{10}} - 0.45\right)^2 = 0.65^2.\end{aligned} \quad (1)$$

The $z \sim 1.5$ boundaries are

$$\begin{aligned}\text{inner:}\ &\left(\log\frac{S_{21}}{S_{10}} - 0.49\right)^2 + \left(\log\frac{S_{18}}{S_{12.8}} - 0.18\right)^2 = 0.21^2\\ \text{outer:}\ &\left(\log\frac{S_{21}}{S_{10}} - 0.60\right)^2 + \left(\log\frac{S_{18}}{S_{12.8}} - 0.03\right)^2 = 0.65^2.\end{aligned} \quad (2)$$

The $z \sim 2$ boundaries are

$$\begin{aligned}\text{inner:}\ &\left(\log\frac{S_{18}}{S_{10}} - 0.43\right)^2 + \left(\log\frac{S_{21}}{S_{15}} - 0.18\right)^2 = 0.18^2\\ \text{outer:}\ &\left(\log\frac{S_{18}}{S_{10}} - 0.50\right)^2 + \left(\log\frac{S_{21}}{S_{15}} - 0.12\right)^2 = 0.52^2.\end{aligned} \quad (3)$$

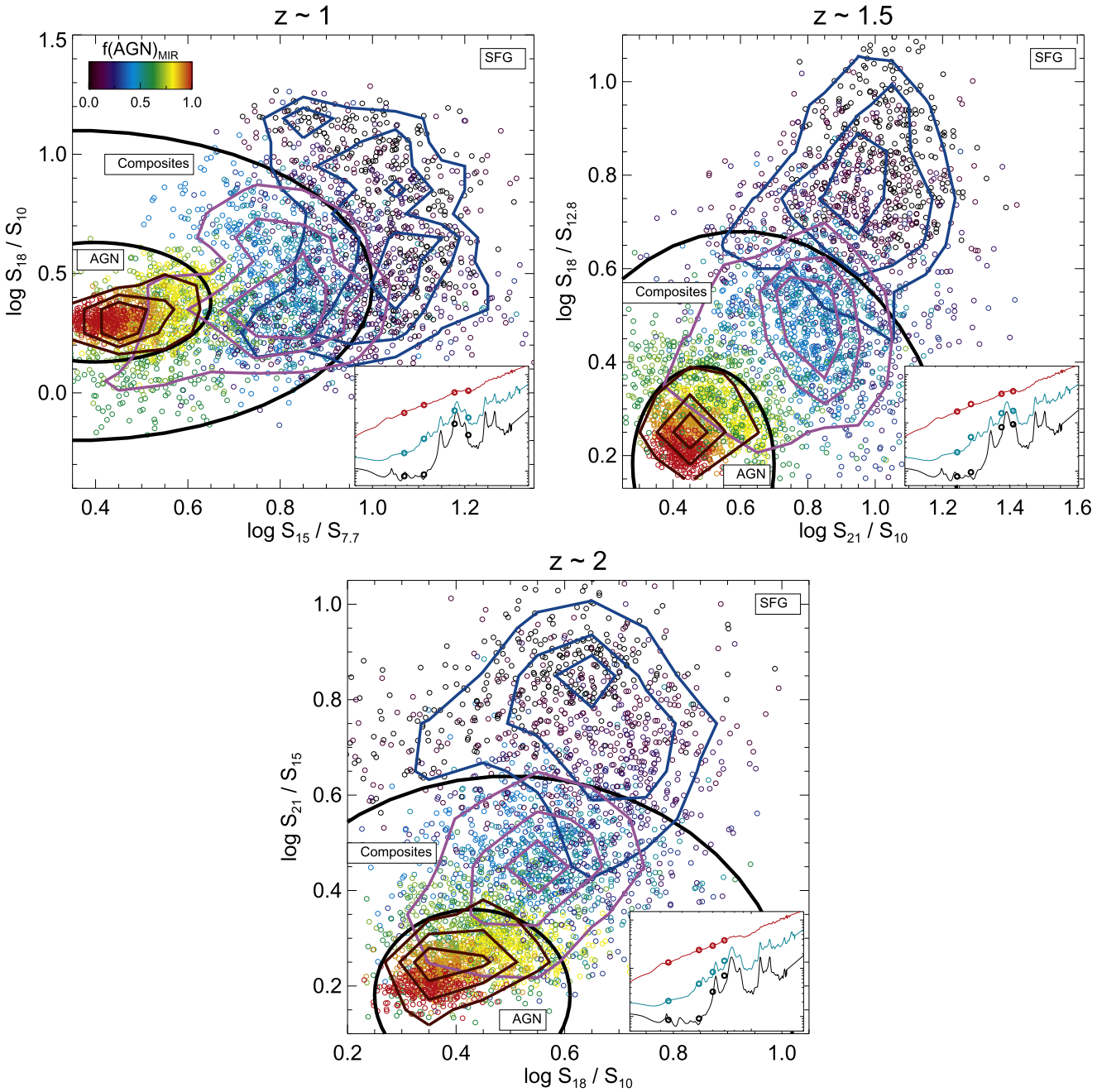

Figure 2. Optimal MIRI color combination for separating Composites, AGNs, and SFGs from $z = 0.75$–1.25 (top left), $z = 1.25$–1.75 (top right), and $z = 1.75$–2.25 (bottom). We show the synthetic galaxies (shaded according to $f(\mathrm{AGN})_{\mathrm{MIR}}$) created from the Kirkpatrick et al. (2015) library used to determine the best AGN and Composite selection regions (black lines), based on completeness and reliability. We also overplot the contours of all the synthetic galaxies classified as SFGs (blue lines), Composites (purple lines), and AGNs (maroon lines) to allow easier viewing of where each category predominantly lies. In the bottom right corner of each diagram, we demonstrate where the photometry filters fall on an SFG (black), Composite (blue), and AGN (red) template at $z = 1$, 1.5, 2.

Table 2
Completeness (Reliability) of MIRI Color Selection

Region	$z \sim 1$	$z \sim 1.5$	$z \sim 2$
AGN	87 (90)%	87 (89)%	87 (80)%
Composite	77 (72)%	79 (74)%	71 (71)%
SFG	76 (81)%	81 (86)%	79 (89)%

These regions are useful for broadly classifying large numbers of sources or identifying targets for follow-up observations. We use these regions to assess the reliability and completeness of our color diagnostic, where again we classify all synthetic sources as SFGs when $f(\mathrm{AGN})_{\mathrm{MIR}} < 0.3$, Composites when $0.3 \leqslant f(\mathrm{AGN})_{\mathrm{MIR}} < 0.7$, and AGNs when $0.7 \geqslant f(\mathrm{AGN})_{\mathrm{MIR}}$. Table 2 lists these values for all three redshift regimes. Comparison with Table 1 shows an improvement over what we were able to reliably classify with the *Herschel* and *Spitzer* diagnostics, particularly for separating Composites from SFGs. The spacing of the MIRI filters allows us to sensitively trace the strength of the PAH features relative to the stellar minimum, where the proportionate amount of PAH emission will be lower for Composite galaxies as the

power-law emission from the AGN begins to outshine the stellar minimum (see the insets in Figure 2 for a visual guide).

Perhaps, instead of broad classifications, the reader would rather have an estimate of $f(\mathrm{AGN})_{\mathrm{MIR}}$. Without mid-IR spectroscopy, robust decomposition into an AGN and star-forming component still is not feasible, even with six photometry filters. However, we have determined how to linearly combine the colors in each redshift regime in order to estimate $f(\mathrm{AGN})_{\mathrm{MIR}}$, and we also measure the standard deviation (σ_{AGN}) of the residuals when each equation is applied to our synthetic sources so that the reader has a measure of the uncertainty. At $z \sim 1$,

$$f(\mathrm{AGN})_{\mathrm{MIR}} = -0.97 \times \left(\log \frac{S_{15}}{S_{7.7}}\right) - 0.10 \times \left(\log \frac{S_{18}}{S_{10}}\right) + 1.29 \quad (4)$$

and $\sigma_{\mathrm{AGN}} = 0.15$.

At $z \sim 1.5$,

$$f(\mathrm{AGN})_{\mathrm{MIR}} = -0.56 \times \left(\log \frac{S_{21}}{S_{10}}\right) - 0.85 \times \left(\log \frac{S_{18}}{S_{12.8}}\right) + 1.29 \quad (5)$$

and $\sigma_{\mathrm{AGN}} = 0.13$.

At $z \sim 2$,

$$f(\mathrm{AGN})_{\mathrm{MIR}} = -0.55 \times \left(\log \frac{S_{18}}{S_{10}}\right) - 1.01 \times \left(\log \frac{S_{21}}{S_{15}}\right) + 1.25 \quad (6)$$

and $\sigma_{\mathrm{AGN}} = 0.16$.

4.1. AGN Contributions in Individual Bands

If we have a good understanding of the typical full IR SED of high-redshift galaxies, as well as the scatter in the population, then a single photometric point can be used in conjunction with representative templates to estimate L_{IR} and star formation rates (SFRs). Since PAH molecules are illuminated by the UV/optical photons from young stars, they are a natural SFR indicator and have been extensively used in the literature to probe SFR and L_{IR} (Peeters et al. 2004; Brandl et al. 2006; Pope et al. 2008; Battisti et al. 2015; Shipley et al. 2016).

Given the coverage of the MIRI filters, we will now examine how an AGN can affect the 7.7 μm PAH feature for the Kirkpatrick et al. (2015) templates used in this work, as any AGN contribution will need to be corrected for before converting a PAH luminosity to an SFR. We remind the reader that for these templates, the AGN component is represented as a power law with a slope of $F_\nu \propto \lambda^{1.5}$. We measure the intrinsic $L_{7.7}$ of each template using PAHFIT (Smith et al. 2007). Then, we measure L_{MIRI}, which is the photometry of the template through the following MIRI filters

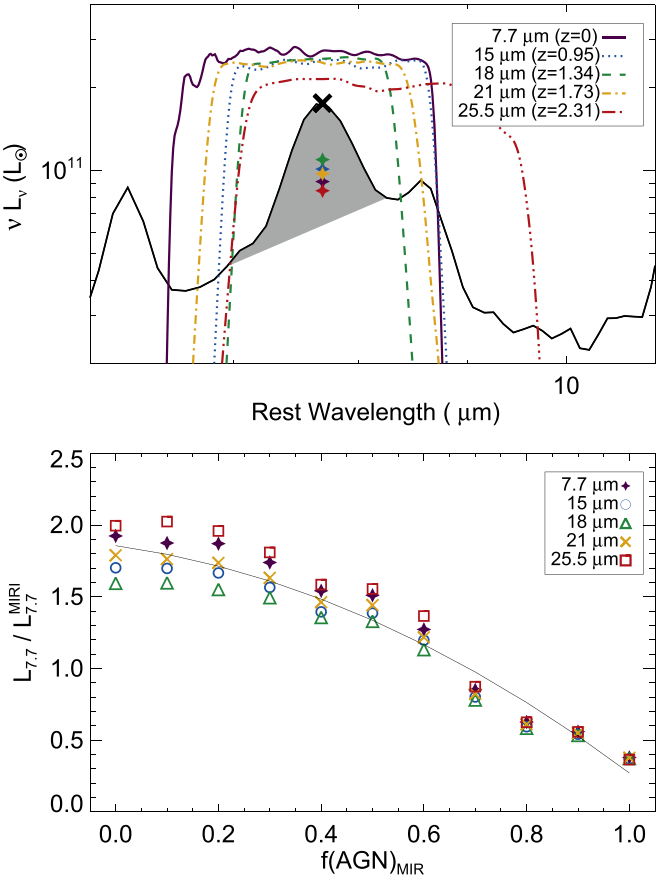

Figure 3. Top panel: we demonstrate, using the MIR0.0 template from Kirkpatrick et al. (2015), how much of the 7.7 μm feature each MIRI filter covers at the redshifts where the central wavelength of each filter is 7.7 μm (listed in the legend). The gray shaded region indicates which part of the spectrum is integrated to calculate $L_{7.7}$ (black cross), while the filled stars show the photometry (in units of νL_ν) measured through each of the MIRI filters. The photometry is lower because it includes more of the spectrum at lower luminosity. Bottom panel: ratio of the MIRI photometry (L_{MIRI}) measured through different MIRI filters depending on redshift to the intrinsic $L_{7.7}$ of the PAH feature. The lower fractions with increasing $f(\mathrm{AGN})_{\mathrm{MIR}}$ are due to an increased warm dust continuum due to heating by an AGN. If $L_{7.7}$ is going to be used to calculate SFRs, corrections need to be made for an AGN contribution. The black line is the empirical relationship between $L_{7.7}/L_{\mathrm{MIRI}}$ and $f(\mathrm{AGN})_{\mathrm{MIR}}$.

at the given redshifts:

$$\begin{aligned} &z = 0,\ 7.7\ \mu\mathrm{m} \\ &z = 0.95,\ 15.0\ \mu\mathrm{m} \\ &z = 1.34,\ 18.0\ \mu\mathrm{m} \\ &z = 1.73,\ 21.0\ \mu\mathrm{m} \\ &z = 2.31,\ 25.5\ \mu\mathrm{m}. \end{aligned} \quad (7)$$

The redshifts mark where the rest-frame central wavelength of each filter is 7.7 μm.

In the top panel of Figure 3, we demonstrate how much of the 7.7 μm feature each filter covers at the above listed redshifts. In the bottom panel, we show the relationship $L_{7.7}/L_{\mathrm{MIRI}}$ as a function of $f(\mathrm{AGN})_{\mathrm{MIR}}$ for each filter at the listed redshifts. The decreasing fractions with increasing $f(\mathrm{AGN})_{\mathrm{MIR}}$ are due to the increased contribution of the warm dust continuum to the measured photometry. We fit a quadratic

relationship to all the points and measure

$$\frac{L_{7.7}}{L_{\rm MIRI}} = (-1.09 \pm 0.20) \times f({\rm AGN})^2_{\rm MIR} - (0.50 \pm 0.21) \times f({\rm AGN})_{\rm MIR} + (1.86 \pm 0.04). \quad (8)$$

This equation, in conjunction with estimating $f({\rm AGN})_{\rm MIR}$ from MIRI colors, can be used for first-order corrections to $L_{7.7}$ before converting to an SFR. Similarly, in Kirkpatrick et al. (2015) we demonstrated that there is a quadratic relationship between $f({\rm AGN})_{\rm MIR}$ and the total contribution of an AGN to $L_{\rm IR}$ that can be used to correct $L_{\rm IR}$ for AGN emission:

$$f({\rm AGN})_{\rm IR} = 0.66 \times f({\rm AGN})^2_{\rm MIR} - 0.035 \times f({\rm AGN})_{\rm MIR}, \quad (9)$$

where $f({\rm AGN})_{\rm IR}$ is the fraction of $L_{\rm IR}$(8–1000 μm) due to AGN heating. Then, the portion of $L_{\rm IR}$ due to star formation is $L_{\rm IR}^{\rm SF} = L_{\rm IR} \times (1 - f({\rm AGN})_{\rm IR})$. Once the AGN contribution is accounted for, $L_{\rm IR}$ can be converted to an SFR using standard equations (e.g., Murphy et al. 2011). For a strong AGN ($f({\rm AGN})_{\rm MIR} \geqslant 0.9$), at least 50% of $L_{\rm IR}$ needs to be removed before converting to an SFR, and the same is true if using 7.7 μm to calculate SFR. Then, the strongest AGN will have SFRs that are overestimated by at least a factor of 2 if not properly accounted for. Of more concern is Composites, which are routinely misidentified as SFGs. For a Composite with $f({\rm AGN})_{\rm MIR} = 0.5$, an $L_{\rm IR}$-based SFR will be overestimated by ~15%. But, if one uses $L_{7.7}$, then the resulting SFR will be overestimated by ~35%.

5. Additional Mid-IR Considerations

5.1. Metallicity and Obscuration

At cosmic noon, the bulk of the star formation is occurring in massive, dusty galaxies with $M_* > 10^{10}\,M_\odot$ (e.g., Murphy et al. 2011; Madau & Dickinson 2014; Pannella et al. 2015), which is the type of galaxy that our MIRI diagnostics were created from (Kirkpatrick et al. 2012, 2015; Sajina & Yan et al. 2012). For studying the AGN–star formation connection, we expect these types of galaxies to form the most appealing targets. Nevertheless, the sensitivity of *JWST*/MIRI will enable studies of lower-mass galaxies, which tend to have lower metallicities (Ma et al. 2016, and references therein). Decreasing gas phase metallicities have been linked with decreasing PAH strengths (e.g., Engelbracht et al. 2008; Sandstrom et al. 2012; Shivaei et al. 2017), which is a source of concern since we are effectively detecting AGN hosts based on the strength of PAH features compared with the stellar minimum at 3–5 μm. Shipley et al. (2016) find that below $Z < 0.7\,Z_\odot$ PAH emission no longer scales linearly with $L_{\rm IR}$, which, based on the mass–metallicity relation, could be a source of concern for contamination of our Composite regions at $M_* < 3 \times 10^9\,M_\odot$, up to $z \sim 2.3$ (Erb et al. 2006; Zahid et al. 2013; Sanders et al. 2015). Recently, using the MOSDEF optical spectroscopic survey, Shivaei et al. (2017) found that at $z \sim 2$ $L_{7.7}/L_{\rm IR}$ is lower for galaxies with $M_* < 10^{10}\,M_\odot$ with a behavior similar to that seen for local galaxies (Engelbracht et al. 2008; Shipley et al. 2016).

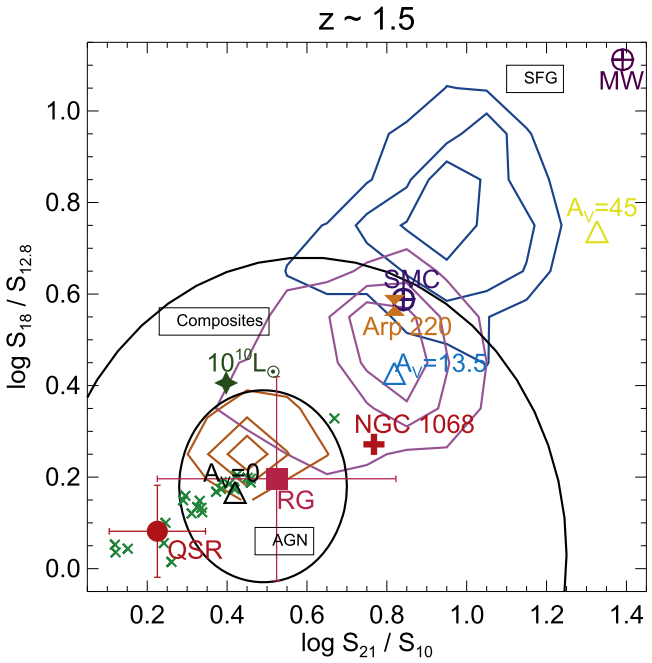

Figure 4. We use our $z \sim 1.5$ MIRI diagnostic to explore where sources with different luminosities, metallicities, and obscurations from the Kirkpatrick et al. (2015) library will lie in color space; we show the distribution of our synthetic SFGs (blue), Composites (purple), and AGNs (orange), as well as the black lines marking the AGN, Composite, and SFG regions. We use the Draine & Li (2007) library to calculate where an SMC galaxy (dark purple circle with cross) and the Milky Way with a lower PAH fraction (purple circle with cross) will lie. The SMC galaxy lies in the Composite region, as well as a galaxy with $L_{\rm IR} = 10^{10}\,L_\odot$ (dark green star) from the Rieke et al. (2009) library. Our diagnostics were calibrated using galaxies with $L_{\rm IR} > 10^{11}\,L_\odot$ and $M_* > 10^{10}\,M_\odot$, so they should be applied with caution to lower-mass, lower-luminosity objects. We also look at what effect obscuration may have on our ability to detect AGNs using local obscured ultraluminous infrared galaxy (ULIRG) Arp 220 (orange bowtie) and Compton-thick AGN NGC 1068 (red cross), both of which lie in the Composite region. We use the IRS spectra of optically selected AGNs at $z > 0.3$ (green crosses) from Hernán-Caballero et al. (2015) to show that a range of AGNs lie in our defined region and to the lower left. Additionally, the empirical quasar template (red circle) and radio galaxy template (pink square) from Leipski et al. (2010) also lie in or below our AGN region. Finally, we use the AGN template library (triangles) of Siebenmorgen et al. (2015) to show how obscuration in the torus (measured in A_V) combined with a large viewing angle (in this case, 67°) and high cloud filling factor will push AGNs into the Composite and SFG region.

At $z \sim 2$, a main-sequence galaxy with $M_* = 10^{10}\,M_\odot$ will have an SFR of ~45 $M_\odot\,{\rm yr}^{-1}$ (Rosario et al. 2013). At $z \sim 2$, 21 μm is tracing the 7.7 μm PAH feature, so applying Equation (11) from Shipley et al. (2016) for this SFR gives $S_{21} \approx 30$ μJy, which is achievable in 7 minutes for a 10σ detection. An hour of integration time at 21 μm will produce 10σ detections of galaxies at roughly 8 μJy, corresponding to $M_* \sim 3 \times 10^9\,M_\odot$, which is well below the threshold where we expect that low-metallicity galaxies might contaminate the Composite regime. As such, our color diagnostics may require recalibration for low-metallicity galaxies when using observations below $S_{21} \lesssim 30$ μJy.

As a visual check, we demonstrate in Figure 4 where SFGs with different PAH strengths will lie in our $z \sim 1.5$ diagnostic. To accomplish this, we use the Small Magellanic Cloud (SMC) dust model (PAH fraction $q_{\rm PAH} = 0.10\%$) and a Milky Way dust model with $q_{\rm PAH} = 0.47\%$ from Draine & Li (2007), which is included to show where a galaxy with a low SFR will

lie. The Draine & Li (2007) models are also parameterized in terms of the strength of the radiation field, $U_{\rm min}$ and $U_{\rm max}$. We set these values to $U_{\rm min} = 1$ and $U_{\rm max} = 1e5$, although these parameters have little effect on the final colors. Also, we note that we add in a stellar blackbody with $T = 5000$ K to complete the near-IR portion of the spectrum. Even with a low PAH fraction, the Milky Way template still lies in our SFG region, while the SMC template lies directly on the Composite/SFG border. Haro 11, another well-studied low-metallicity galaxy ($Z = 1/3\ Z_{\odot}$; James et al. 2013) in the nearby universe, has nearly identical MIRI colors to our plotted SMC data point, further confirming that low-metallicity galaxies will likely lie around the Composite/SFG border. The reason is that even though low-metallicity galaxies have diminished PAH features, they still have a deep and broad stellar minimum at 3–5 μm (Lyu et al. 2016), unlike Composites, which begin to exhibit the warmer dust characteristic of the AGN torus. We also plot the template from Rieke et al. (2009), which corresponds to an $L_{\rm IR} = 10^{10}\ L_{\rm IR}$, as this is an order of magnitude less luminous than the Kirkpatrick et al. (2015) library. A galaxy of this luminosity also lies in the Composite region, although it is away from the locus of our Composite galaxies (purple distribution).

We caution the reader to be prudent when classifying galaxies as Composites, particularly low-mass sources that lie near the Composite and SFG border. If stellar masses of MIRI samples are known (possibly through NIRcam observations), low-mass galaxies that lie in our Composite regions provide excellent targets for follow-up spectroscopy observations, to distinguish between AGNs and metallicity as the underlying cause of the diminished PAH emission.

The other prominent concern in a mid-IR diagnostic is how obscuration can affect the detection of AGNs. Our template library was built assuming that the AGN can be represented as a power law, and we empirically measure the power-law component to have an average slope of $F_{\nu} \propto \lambda^{1.5}$, but individual sources will show a range of slopes and a range of dust obscurations. The AGN templates in the Kirkpatrick et al. (2015) library are derived from AGNs where 75% of the sample are also detected in the X-ray, implying that they are largely unobscured. Of the Composite sources in Kirkpatrick et al. (2015), only 35% are X-ray detected, indicating that they contain more heavily obscured AGNs. We now explore the effects of dust obscuration by examining where different galaxies will lie in the $z \sim 1.5$ color space (Figure 4).

Arp 220 (orange bowtie) is a local ULIRG that is heavily dust obscured and may host an AGN (Veilleux et al. 2009; Teng et al. 2015). Its position near the SMC and at the edge of the Composite region indicates another possible ambiguity, that the aromatic bands tend to be suppressed in the most luminous and compact infrared galaxies. How many such objects exist at cosmic noon is not well quantified, as most galaxies of the same luminosity as local ULIRGs ($L_{\rm IR} > 10^{12}\ L_{\odot}$) have extended ISMs (Papovich et al. 2009; Younger et al. 2009; Finkelstein et al. 2011; Rujopakarn et al. 2011; Ivison et al. 2012; Rujopakarn et al. 2016). NGC 1068 (red cross) is an archetypal local Compton-thick Seyfert II AGN. Despite its extreme obscuration, it lies securely in our Composite region, close to the AGN boundary.

The AGNs that our templates were composed of all have remarkable similar mid-IR spectral slopes. To more fully explore the *JWST* colors expected of AGNs, we include two literature samples. First, Hernán-Caballero et al. (2015) have *Spitzer*/IRS spectra for 189 low-redshift optically selected AGNs. Of these, 24 have $z > 0.3$, so the IRS spectrum covers the appropriate wavelength range for our MIRI diagnostic. These galaxies are shown as the green crosses in Figure 4. They all lie either in our AGN region (with the exception of one galaxy) or to the lower left. Next, we look at the quasar and radio galaxy templates from Leipski et al. (2010). These templates were created from 11 quasars and 9 radio galaxies, respectively, at $1.0 < z < 1.4$. The radio galaxies are dust obscured with an average $\tau_{9.7\ \mu{\rm m}} = 1.1$. In fact, the radio galaxy template has the same shape as the quasar template viewed through a dust screen with $A_V = 20$. The radio galaxy template (pink square) lies in our AGN region, although the 1σ dispersion of the sources used to create the template indicates a range of colors that bleeds into our Composite region. The quasar template (red circle) lies to the lower left, and the 1σ dispersion is relatively small. Indeed, both the quasar template and some of the IRS AGN spectra lie in a region not occupied by any of our synthetic galaxies (represented by the contours). Sources that lie to the lower left of our AGN regions in any of our diagrams are then most probably bright AGNs.

We also use the AGN library of Siebenmorgen et al. (2015) to examine what extinction conditions would push an AGN into our SFG region. These AGN templates are calculated assuming that the AGN IR emission arises from a two-phase dust region consisting of a torus and disk, torus radius (R), viewing angle, cloud filling factor (V_c), optical depth of clouds in the torus (A_V), and optical depth of the disk midplane (A_d). Viewing angle alone can push an AGN into our SFG region, if the angle is greater than 80°. For viewing angles greater than 60°, a high cloud optical depth ($A_V \geqslant 13.5$) and high filling factor ($V_c > 38\%$) can also push pure AGNs into the Composite and SFG regions. We demonstrate how a pure AGN, with no stellar component, can mimic the colors of Composites and SFGs with increasing cloud

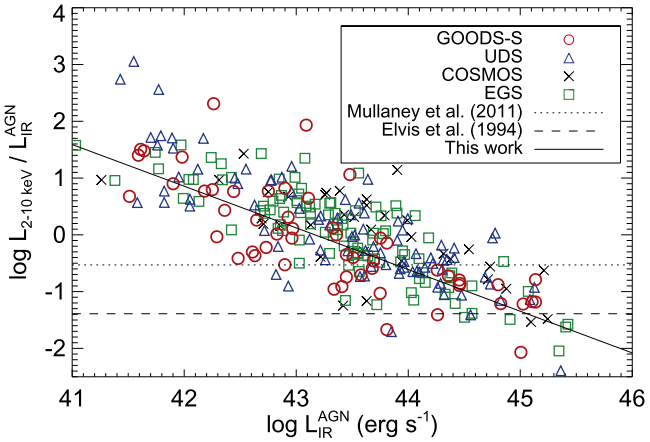

Figure 5. $L_{2-10\,{\rm keV}}/L_{\rm IR}^{\rm AGN}$ as a function of $L_{\rm IR}^{\rm AGN}$ (all quantities are in erg s^{-1}) for the four CANDELS fields. We empirically measure the relationship (solid line) using only the GOODS-S data (red circles), since this is the field where the *Chandra* observations are complete down to $L_{2-10\,{\rm keV}} = 10^{42}$ erg s^{-1} out to $z = 2$. We show the approximate conversions derived in Mullaney et al. (2011; dotted line), using a local sample of AGNs with $L_{2-10\,{\rm keV}} \sim 10^{43}$ erg s^{-1}, and derived in Elvis et al. (1994; dashed line) from quasars with $L_{2-10\,{\rm keV}} > 10^{45}$ erg s^{-1}.

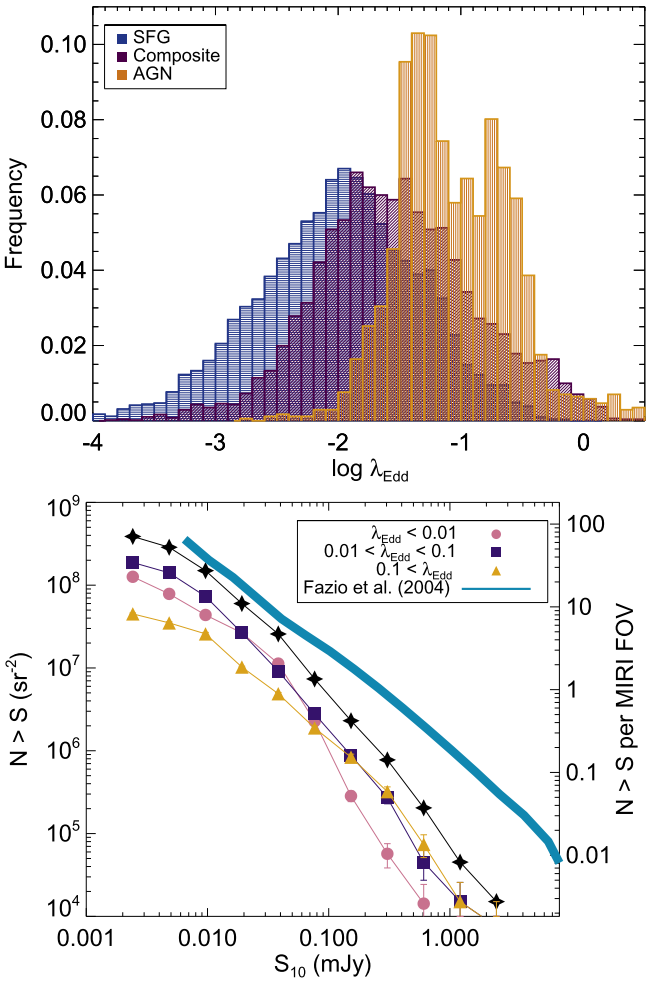

Figure 6. Top panel: we calculate $\lambda_{\rm Edd}$ for CANDELS+COSMOS-identified SFGs (blue), Composites (purple), and AGNs (orange) by applying standard scaling relations to M_*, $f(\rm AGN)_{\rm MIR}$, and $L_{\rm IR}$. We have normalized the distributions to show the relative frequencies in each category. Each category spans an overlapping range, illustrating the current limitations in understanding how observed IR dust emission relates to the accretion on a galaxy's central black hole. Bottom panel: we predict the MIRI 10 μm number counts at $z = 0.75$–2.25 and then break them into bins of $\lambda_{\rm Edd}$. We have scaled the 24 μm emission of the CANDELS and COSMOS galaxies shown in Figure 1 using the appropriate template for SFGs, Composites, and AGNs. Our 10 μm counts agree with the measured 8 μm counts in Fazio et al. (2004; blue line). The discrepancies between the 10 and 8 μm counts can be attributed to the redshift cut. In one MIRI FOV, we will detect nearly 100 galaxies down to 2 μJy, and many of these will be AGN hosts.

optical depth (blue and yellow triangles) for a viewing angle of 67° and $V_c = 77.7\%$ (we use the model with $R = 1545 \times 10^{15}$ cm *and* $A_d = 300$; changes in these parameters are not responsible for causing the AGN to lie in the SFG region). Detecting such an obscured AGN at other wavelengths would also be extremely challenging, and identifying complete samples of true Type II obscured AGNs remains an unsolved problem. Del Moro et al. (2016) find that 30% of mid-IR-luminous quasars at $z \sim 1$–3 in the GOODS-S field are not detected in the *Chandra* 6 Ms data. Of those that are detected, >65% are Compton thick. Beyond these estimates, it is difficult to say how many heavily obscured AGNs there are that would not be selected as such in the X-ray or the mid-IR. Identifying

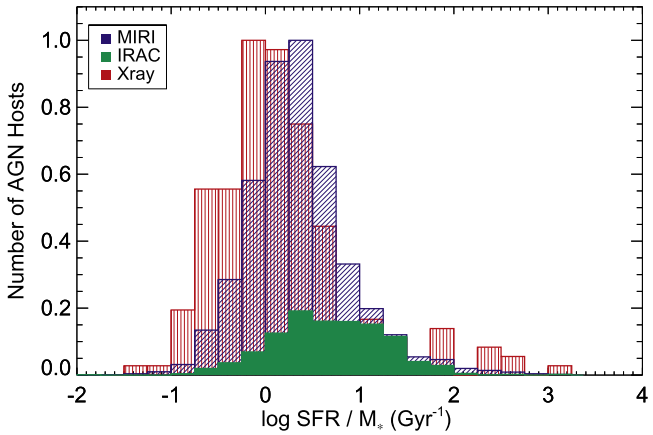

Figure 7. We show the host galaxy property sSFR = SFR/M_* of CANDELS galaxies identified as likely AGNs according to a hard X-ray cut (red histogram; $L_{2-10\,\rm keV} \geqslant 10^{43}$ erg s^{-1}) and MIRI color selection (blue histogram). We have normalized each distribution to allow easier comparison, although the MIRI distribution has 20× more sources. The MIRI selection is sensitive to host galaxies with higher sSFRs. We illustrate which of the MIRI-selected AGN hosts would also be selected with the Donley et al. (2012) IRAC selection criteria. Due to the sensitivity and coverage of the MIRI filters, we will be able to select larger samples of AGN hosts than was possible with IRAC selection.

these very obscured AGNs will require detailed SED modeling using a full suite of NIRcam+MIRI observations, which is beyond the scope of this paper.

5.2. The 3.3 μm PAH Feature

At $z = 1$–2, the PAH 3.3 μm feature will fall into the 7.7 and 10 μm bandpasses, so it is worth considering whether this feature might also be used as an AGN discriminator. As this is a narrow feature, its effect on a photometric measurement will be much less than the broad 7.7 μm complex. For example, Lee et al. (2012) measure the 3.3 μm feature using AKARI near-IR spectra of local (U)LIRGs, and the largest equivalent width the authors measure is 0.18 μm. By comparison, MIRI F770W has $\Delta_\lambda = 2.2$ μm. Then, in the most optimistic scenario, the 3.3 μm feature will span <10% of the broadband photometry filter. Still, if the PAH emission is particularly strong, it may have a measurable effect on the photometry, and an excess may be observed. However, we note that this PAH feature lies adjacent to water absorption at the 3.1 μm, which will also fall in a broadband filter and diminish any excess.

Of more concern is the fact that the 3.3 μm feature is not uniformly observed, in contrast to the 6.2 and 7.7 μm complexes. Sajina et al. (2009) looked for 3.3 μm emission in 11 $z \sim 2$ galaxies and detect it in only four sources. Lee et al. (2012) do not detect the feature in 11 out of 36 local (U) LIRGs. Moreover, in both of those samples, the 3.3 μm feature fails to exhibit a strong anticorrelation with AGN strength. This is because, at this wavelength range, the emission from the torus is beginning to decrease, but the emission from the accretion disk (which can dominate UV/optical light) is also weak (e.g., Calistro Rivera et al. 2016, and references therein). Then, any particularly strong dust features from $\lambda \sim 0.8$–3.5 μm are still visible. In fact, in Sajina et al. (2009), three of the four spectra that exhibit the 3.3 μm emission are all AGNs with $f(\rm AGN)_{\rm MIR} > 0.7$. Of

the 26 sources Lee et al. (2012) detect 3.3 μm emission in, the authors classify 11 as AGNs based on various near-IR spectral features. Taken together, these points argue against the utility of 3.3 μm emission as a color-based discriminator.

6. Discussion: Physical Properties of an MIRI Sample

We now return to our CANDELS+COSMOS sample to investigate the physical properties of galaxies that MIRI color selection will identify as being AGN hosts. $f(\mathrm{AGN})_{\mathrm{MIR}}$ is strictly a measure of the dust heated by an AGN relative to that heated by star formation, so now we examine a more physically motivated quantity, the Eddington ratio. The Eddington ratio is defined as $\lambda_{\mathrm{Edd}} = L_{\mathrm{bol}}/L_{\mathrm{Edd}}$, where L_{bol} is the bolometric luminosity of the AGN and L_{Edd} is the Eddington luminosity. In this way, λ_{Edd} is a measure of how efficiently a black hole is accreting material. L_{bol} is commonly estimated from the hard X-ray luminosity, $L_{2-10\,\mathrm{keV}}$. Due to obscuration and varying depths of the *Chandra* catalogs in the CANDELS fields, we do not have $L_{2-10\,\mathrm{keV}}$ for all of our IR identified AGNs and Composites. As a first step toward calculating L_{bol}, we estimate $L_{2-10\,\mathrm{keV}}$ from $L_{\mathrm{IR}}^{\mathrm{AGN}}$ for all sources. We empirically determine the scaling between these luminosities to be

$$\log\left(\frac{L_{2-10\,\mathrm{keV}}}{L_{\mathrm{IR}}^{\mathrm{AGN}}}\right) = (31.698 \pm 3.535) - (0.734 \pm 0.082) \times \log L_{\mathrm{IR}}^{\mathrm{AGN}}\ [\mathrm{erg\ s^{-1}}] \quad (10)$$

measured directly using *Chandra* observations of the GOODS-S field, which is the only field where the *Chandra* data are complete down to $L_{2-10\,\mathrm{keV}} = 10^{42}$ erg s^{-1} out to $z = 2$ (Xue et al. 2011; Hsu et al. 2014). Note that $L_{2-10\,\mathrm{keV}}$ is the observed luminosity, as in most cases we do not have high enough counts to make a meaningful obscuration measurement. Figure 5 shows this empirically derived relationship, along with the approximate conversion factors derived in Mullaney et al. (2011), using a local sample of AGNs with $L_{2-10\,\mathrm{keV}} \sim 10^{43}$ erg s^{-1}, and derived in Elvis et al. (1994) from quasars with $L_{2-10\,\mathrm{keV}} > 10^{45}$ erg s^{-1}. Our conversion is in line with the literature results for the brighter AGNs.

We then apply Equation (10) to all sources in the CANDELS and COSMOS fields. Next, we convert $L_{2-10\,\mathrm{keV}}$ to L_{bol} using Equation (2) in Hopkins et al. (2007). This equation results in $L_{2-10\,\mathrm{keV}}/L_{\mathrm{bol}} \sim 0.06$–$0.01$, in agreement with direct measurements in the literature (Vignali et al. 2003; Steffen et al. 2006; Vasudevan & Fabian 2007). Finally, we calculate $L_{\mathrm{Edd}}[\mathrm{erg\ s^{-1}}] = 1.3 \times 10^{38} \times M_{\mathrm{BH}}[M_{\odot}]$, where $M_{\mathrm{BH}} = 0.002\,M_{*}$ following the convention in Marconi & Hunt (2003) and Aird et al. (2012).

With the techniques outlined in Section 4, we will be able to calculate λ_{Edd} for samples with M_{*} or M_{BH} measurements. The relationship between λ_{Edd} and $f(\mathrm{AGN})_{\mathrm{MIR}}$ is not linear, since λ_{Edd} depends not only on $f(\mathrm{AGN})_{\mathrm{MIR}}$ but also on L_{IR} and M_{*}. Then, each $f(\mathrm{AGN})_{\mathrm{MIR}}$ can have a range of λ_{Edd} depending on the host galaxy properties. We show in the top panel of Figure 6 the distribution of λ_{Edd} for each galaxy category.

In the bottom panel of Figure 6, we illustrate the predicted number counts at cosmic noon with the MIRI 10 μm filter, which is chosen for its sensitivity ($\sim$0.6 μJy at 10σ in $<$3 hr; Glasse et al. 2015) and because we use it in all three color diagnostics. We calculate the 10 μm flux for all CANDELS +COSMOS galaxies at $z = 0.75$–2.25 and with $M_{*} > 10^{8}\,M_{\odot}$ by scaling the appropriate Kirkpatrick et al. (2015) template (based on the source's $f(\mathrm{AGN})_{\mathrm{MIR}}$ determined through color classification) to the available IR photometry and convolving with the 10 μm transmission filter. By template fitting, we are also able to calculate L_{IR} and $f(\mathrm{AGN})_{\mathrm{IR}}$. The total 10 μm counts are plotted as the black stars in the bottom panel of Figure 6. By including lower-mass galaxies, we push below the 80% completeness in Figure 1 and down to the 20% completeness limit (corresponding to $\sim$40 μJy at 24 μm). For reference, the 80% completeness limit (measured at 24 μm) corresponds to $S_{10} \sim 10$ μJy. Our counts are in good agreement at the faint end with the published 8 μm galaxy counts in Fazio et al. (2004). At the bright end, we have fewer sources owing to the redshift cut we imposed and the small field sizes, similar to our 24 μm number counts in Figure 1.

We also break our 10 μm number counts into bins of λ_{Edd}. Comparison with the top panel demonstrates that the $\lambda_{\mathrm{Edd}} < 0.01$ curve (pink circles) is dominated by SFGs, while the $\lambda_{\mathrm{Edd}} > 0.1$ curve (yellow) has accretion rates typical of sources identified as AGNs at IR and X-ray wavelengths. The majority of the counts are $\lambda_{\mathrm{Edd}} = 0.01$–$0.1$ (purple squares), and these are objects that could be classified as AGNs, SFGs, or Composites.

The MIRI field of view (FOV) is $1\farcm2 \times 1\farcm9$, so we also illustrate the counts in a MIRI FOV on the right axis of Figure 6. We expect nearly 100 objects per MIRI FOV down to 2 μJy at 10 μm, achievable at a signal-to-noise ratio of 10 (5) in roughly 15 minutes (3.6 minutes). Of these objects, $>$50% may be AGN hosts where we can detect and measure the black hole accretion. Below $S_{10} = 10$ μJy, the counts become dominated by sources with $M_{*} < 10^{9}\,M_{\odot}$. Of the galaxies with $\lambda_{\mathrm{Edd}} > 0.01$, 30% have $M_{*} < 10^{9}\,M_{\odot}$ and compose a prime population for follow-up studies to more concretely pin down the AGN fraction in low-mass galaxies at $z \sim 1$–2.

The above analysis was done assuming spatially unresolved galaxies, but the resolution of MIRI may allow for the detection of AGNs in even lower-λ_{Edd} galaxies. For example, at $z = 1$, our color diagnostic requires F1500W, which has a spatial resolution of $0\farcs48$. This resolution corresponds to physical scales of 3.8 kpc. Now, at cosmic noon, M_{BH} is more closely tied to M_{*} rather than bulge mass (e.g., Sun et al. 2015), and very roughly speaking, half of the stellar mass will be contained in the central 3.8 kpc (see size measurements in Rujopakarn et al. 2016). Our color selection can then be applied to just the central resolution element, which is where all of the AGN emission will emanate from. Then, we will be able to detect galaxies with λ_{Edd} that is half of what we have predicted in Figure 6.

The use of the λ_{Edd} parameter highlights an area where MIRI will enable great strides forward, namely, understanding how the observable properties of AGN hosts correlate to their physical properties. The broad distributions of λ_{Edd} in the top panel of Figure 6 demonstrate the limitations of either broadly grouping sources into AGNs, Composites, and SFGs based on observables or using scaling relations to calculate physical properties, or very likely a combination of the two. But with the high-resolution

spectroscopy on MIRI and the increased number of photometric filters, we will be able to classify galaxies on the relative strengths of PAH features, estimate $f(\mathrm{AGN})_{\mathrm{MIR}}$, and combine with M_* (attainable with NIRcam) to measure λ_{Edd}, providing clearer insight into the relationship between galaxy dust emission and black hole accretion.

Finally, we demonstrate the host galaxy properties of CANDELS AGNs and Composites selected with different techniques at $z \sim 1$–2 in Figure 7. We calculate SFR for all galaxies by fitting templates from the Kirkpatrick et al. (2015) library, based on classification as an SFG, Composite, or AGN, and then removing the AGN contribution to L_{IR} before converting to an SFR using Equation (3) in Kennicutt (1998). We combine SFR with M_* (Santini et al. 2015; Stefanon et al. 2017) to measure sSFR $=$ SFR$/M_*$, a common probe of galaxy evolution, as this ratio will be lower in galaxies that are quenching (e.g., Pandya et al. 2017, and references therein). In red, we plot the distribution of specific SFR (sSFR) for those galaxies identified as AGNs in the hard X-ray band ($L_{2-10\,\mathrm{kev}} \geqslant 10^{43}$ erg s^{-1}). Then, we plot the distribution of sSFR in blue for those galaxies that will be selected as either AGNs or Composites by our MIRI color diagnostics, based on our estimation of their *JWST* colors through template fitting. For easier comparison, we normalize both distributions to have a peak at 1, although the MIRI distribution actually has 20× more galaxies than the X-ray distribution. In practice, the relative numbers of X-ray and MIRI AGNs will depend on the depth of the observations and the area covered, but the sensitivity of MIRI and our ability to select Composite sources will enable larger samples than X-ray selection alone. Crucially, our cosmic noon CANDELS AGN hosts have higher sSFR than the X-ray-selected CANDELS galaxies (Azadi et al. 2015; Mullaney et al. 2015). Combining MIRI and X-ray samples will increase our dynamic range in sSFR, allowing us to explore how black hole accretion varies with star formation and main-sequence location (Mullaney et al. 2012; Rosario et al. 2013; Stanley et al. 2015).

Prior to *JWST*, the most popular way of identifying large samples of IR AGNs is with IRAC color techniques (Lacy et al. 2004; Stern et al. 2005; Donley et al. 2012). The Donley et al. (2012) IRAC diagnostic is the most reliable, since it eliminates host galaxy contamination, but it is only sensitive to the most actively accreting AGN as it is based on a power-law selection criterion. Hence, it is likely to be significantly incomplete for Compton-thick and other obscured AGNs. Of the CANDELS sources selected by our MIRI diagnostics, we show in green the sources that are also selected as AGNs by the Donley et al. (2012) criteria. Clearly, due to the sensitivity and spacing of the MIRI filters, we will be able to detect >4 times as many AGN hosts as would be identified with IRAC alone. MIRI color selection will enable identification of statistical samples of AGN hosts in their star-forming prime (as measured by sSFR), allowing astronomers to trace the star formation–AGN connection at the peak period of stellar and black hole growth in the universe.

7. Conclusions

We identify SFGs, AGN, and Composites in four CANDELS fields and in the full COSMOS field using three different redshift-dependent color identification techniques. We present the first 24 μm counts of star-forming+AGN Composite galaxies at $z \sim 1$–2. We find that IR AGNs and Composites dominate 24 μm samples at $S_{24} > 0.8$ mJy. Any 24 μm selected sample contains >25% of Composites.

We use a library of SFG, AGN, and Composite templates to create synthetic galaxies, and we use these synthetic galaxies to create *JWST*/MIRI color selection techniques for three redshift bins, $z \sim 1$, $z \sim 1.5$, and $z \sim 2$. Our techniques can safely be applied to galaxies with $M_* > 10^{10}\,M_\odot$. However, below this regime, metallicity may effect the strength of the PAH features, causing contamination of our Composite regime. MIRI can achieve 10σ detections of $M_* < 10^{10}\,M_\odot$ galaxies out to $z \sim 2$ in a matter of minutes, so future *JWST* observations will prove crucial in separating differences in mid-IR emission due to metallicity rather than AGNs in low-mass galaxies.

At these redshifts, our color selection techniques cover the 6.2 and 7.7 μm PAH features and the 3–5 μm stellar minimum, which are robust tracers of star formation. We demonstrate how to correct $L_{7.7}$ for AGN contamination before converting to an SFR, a crucial step or SFRs based on 7.7 μm PAH emission will be overestimated by >50% for AGNs and 35% for Composites.

Finally, we predict the Eddington ratios (λ_{Edd}), a measure of black hole accretion efficiencies, that we will observe with MIRI imaging. Our MIRI color selection diagnostic can identify samples of AGNs and Composite galaxies with $\lambda_{\mathrm{Edd}} > 0.01$ that are four times larger than samples of AGNs selected by *Spitzer*/IRAC techniques. We also use our new 24 μm number counts to predict the number counts at 10 μm in different bins of λ_{Edd}. With MIRI color identification, we will be able to probe the star formation–AGN connection in dusty galaxies at cosmic noon.

A.K. thanks Sandy Faber and Belinda Wilkes for helpful conversations. A.K. gratefully acknowledges support from the YCAA Prize Postdoctoral Fellowship. A.P. and A.S. acknowledge NASA ADAP13-0054 and NSF AAG grants AST-1312418 and AST-1313206.

Appendix

In this appendix we show our redshift-dependent color diagnostic to find SFGs, Composites, and AGNs using *Spitzer* and *Herschel* photometry. We create a catalog of 5500 synthetic galaxies from 11 templates where we know the intrinsic AGN contribution. We resample each photometric point within the uncertainties of the template from which it was created, so that we can represent the scatter in color space of real galaxies, which is an improvement on using so-called redshift tracks alone to explore where SFGs, Composites, and AGNs lie in color space.

We create color diagrams in redshift bins of $z = 0.75$–1.25, $z = 1.25$–1.75, and $z = 1.75$–2.25. In each redshift bin, we divide the color space into regions of 0.2×0.2 dex and calculate the average $f(\mathrm{AGN})_{\mathrm{MIR}}$ and standard deviation σ_{AGN} of all the synthetic galaxies that lie in that region. In Figures 8–10 below, we show our three diagnostics: S_{250}/S_{24} versus $S_8/S_{3.6}$, S_{100}/S_{24} versus $S_8/S_{3.6}$, and S_{24}/S_8 versus $S_8/S_{3.6}$.

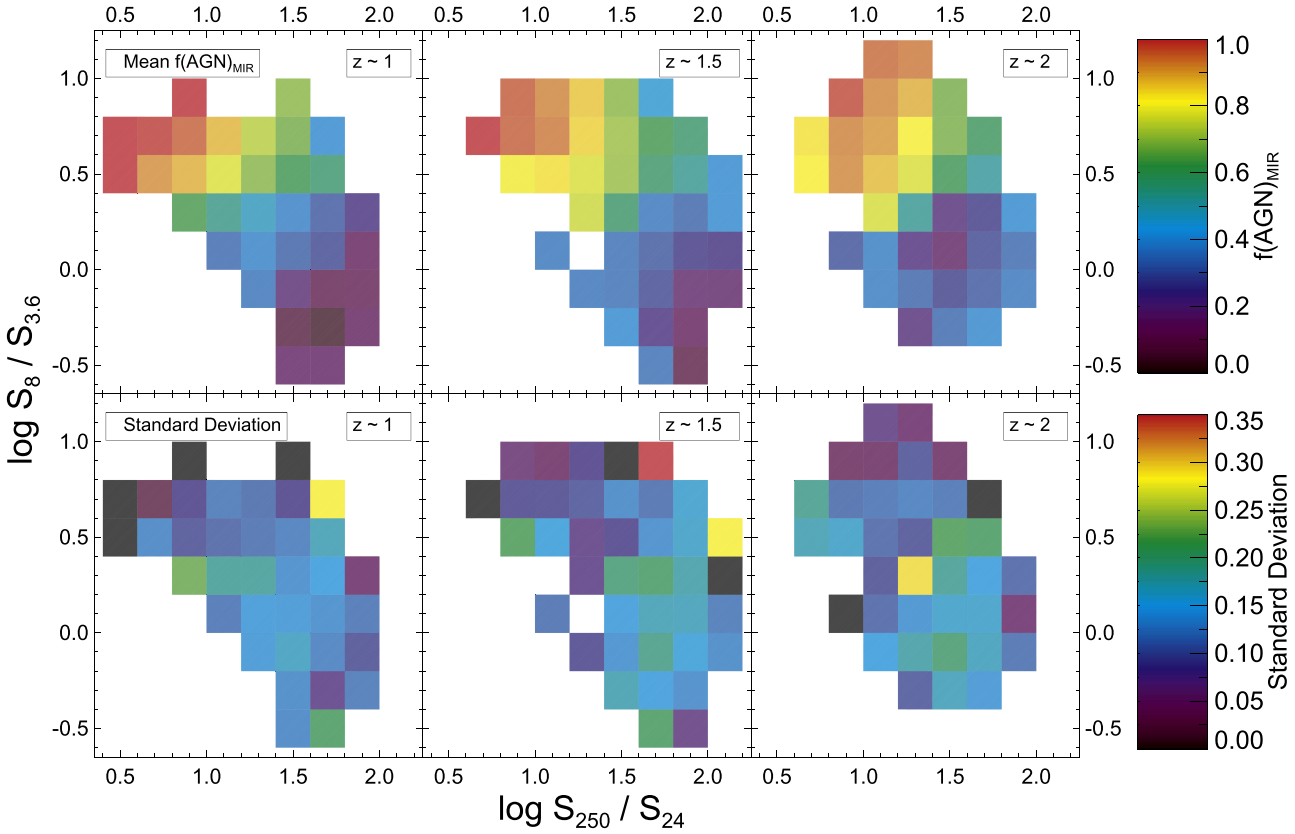

Figure 8. S_{250}/S_{24} vs. $S_8/S_{3.6}$ in three redshift bins. The top panels are shaded according to the average $f(\mathrm{AGN})_{\mathrm{MIR}}$ measured in each bin, and the bottom panels show the standard deviation of $f(\mathrm{AGN})_{\mathrm{MIR}}$ for the sources in each bin.

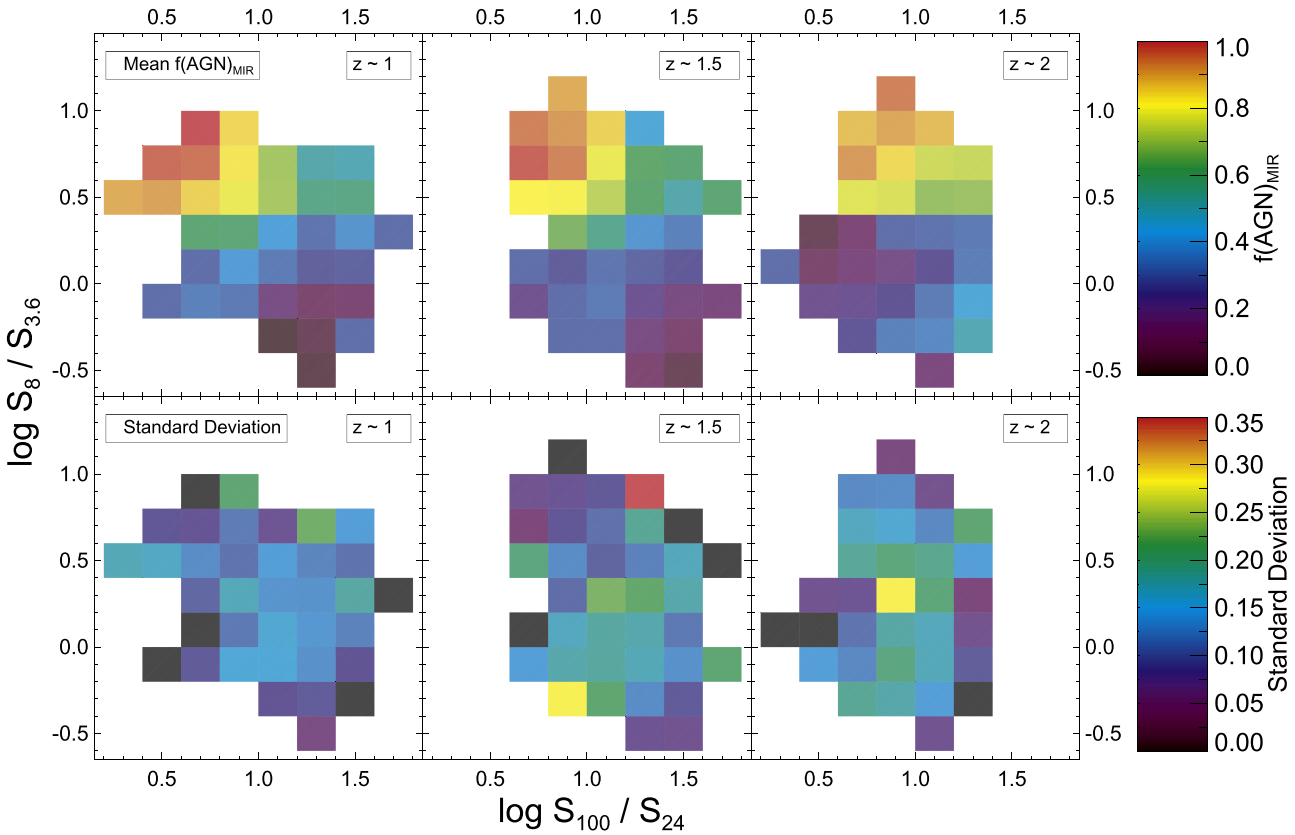

Figure 9. S_{100}/S_{24} vs. $S_8/S_{3.6}$ in three redshift bins. The top panels are shaded according to the average $f(\mathrm{AGN})_{\mathrm{MIR}}$ measured in each bin, and the bottom panels show the standard deviation of $f(\mathrm{AGN})_{\mathrm{MIR}}$ for the sources in each bin.

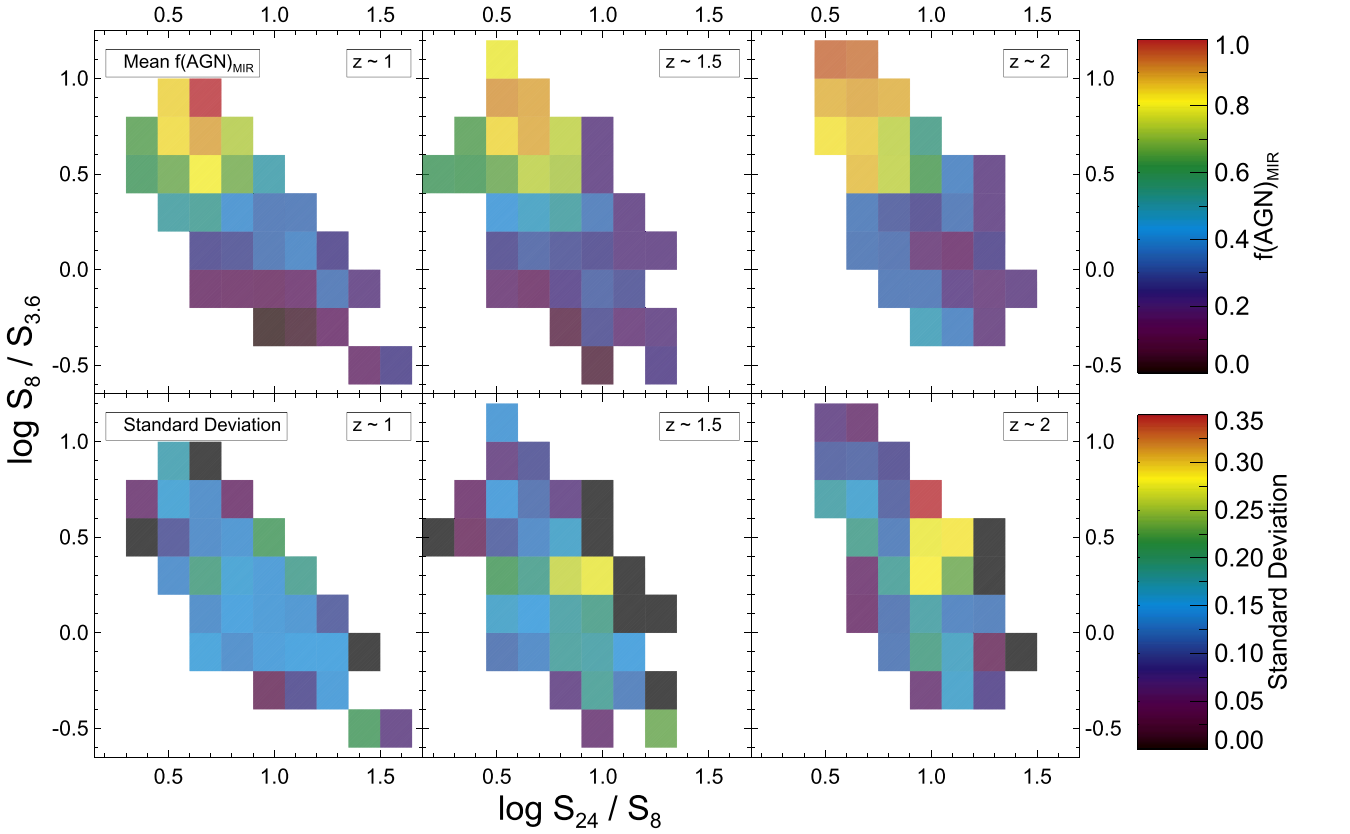

Figure 10. S_{24}/S_8 vs. $S_8/S_{3.6}$ in three redshift bins. The top panels are shaded according to the average $f(\mathrm{AGN})_{\mathrm{MIR}}$ measured in each bin, and the bottom panels show the standard deviation of $f(\mathrm{AGN})_{\mathrm{MIR}}$ for the sources in each bin.

ORCID iDs

Allison Kirkpatrick https://orcid.org/0000-0002-1306-1545
Alexandra Pope https://orcid.org/0000-0001-8592-2706
Guillermo Barro https://orcid.org/0000-0001-6813-875X
George H. Rieke https://orcid.org/0000-0003-2303-6519
Lucia Rodríguez-Muñoz https://orcid.org/0000-0002-0192-5131
Anna Sajina https://orcid.org/0000-0002-1917-1200
Norman A. Grogin https://orcid.org/0000-0001-9440-8872
Viraj Pandya https://orcid.org/0000-0002-2499-9205
Mara Salvato https://orcid.org/0000-0001-7116-9303
Paola Santini https://orcid.org/0000-0002-9334-8705

References

Aird, J., Coil, A., Moustakas, J., et al. 2012, ApJ, 746, 90
Alonso-Herrero, A., Pérez-González, P. G., Alexander, D. M., et al. 2006, ApJ, 640, 167
Azadi, M., Aird, J., Coil, A. L., et al. 2015, ApJ, 806, 187
Battisti, A. J., Calzetti, D., Johnson, B. D., & Elbaz, D. 2015, ApJ, 800, 143
Bonato, M., Sajina, A., De Zotti, G., et al. 2017, ApJ, 836, 171
Bouchet, García-Marín, M., Lagage, P.-O., et al. 2015, PASP, 127, 612
Brand, K., Dey, A., Weedman, D., et al. 2006, ApJ, 644, 143
Brandl, B. R., Bernard-Salas, J., Spoon, H. W. W., et al. 2006, ApJ, 653, 1129
Calistro Rivera, G., Lusso, E., Hennawi, J. F., & Hogg, D. W. 2016, ApJ, 833, 98
Coppin, K., Pope, A., Menéndez-Delemstre, K., et al. 2010, ApJ, 713, 503
Dahlen, T., Mobasher, B., Faber, S. M., et al. 2013, ApJ, 775, 93
Del Moro, A., Alexander, D. M., Bauer, F. E., et al. 2016, MNRAS, 456, 2105
Donley, J. L., Koekemoer, A. M., Brusa, M., et al. 2012, ApJ, 748, 142
Draine, B. T., & Li, A. 2007, ApJ, 657, 810
Elvis, M., Wilkes, B. J., McDowell, J. C., et al. 1994, ApJS, 95, 1
Engelbracht, C. W., Rieke, G. H., Gordon, K. D., et al. 2008, ApJ, 685, 678
Erb, D. K., Shapley, A. E., Pettini, M., et al. 2006, ApJ, 644, 813
Fazio, G. G., Ashby, M. L. N., Barmby, P., et al. 2004, ApJS, 154, 39
Finkelstein, K. D., Papovich, C., Finkelstein, S. L., et al. 2011, ApJ, 742, 108
Glasse, Rieke, G. H., Bauwens, E., et al. 2015, PASP, 127, 686
Hernán-Caballero, A., Alonso-Herrero, A., Hatziminaoglou, E., et al. 2015, ApJ, 803, 109
Hickox, R. C., & Markevitch, M. 2007, ApJ, 661, 117
Hopkins, P. F., Hernquist, L., Cox, T. J., et al. 2006, ApJS, 163, 1
Hopkins, P. F., Richards, G. T., & Hernquist, L. 2007, ApJ, 654, 731
Hsu, L.-T., Salvato, M., Nandra, K., et al. 2014, ApJ, 796, 60
Ivison, R. J., Smail, I., Amblard, A., et al. 2012, MNRAS, 425, 1320
James, B. L., Tsamis, Y. G., Walsh, J. R., Barlow, M., & Westmoquette, M. S. 2013, MNRAS, 430, 2097
Kennicutt, R. C., Jr. 1998, ApJ, 498, 541
Kirkpatrick, A., Pope, A., Alexander, D. M., et al. 2012, ApJ, 759, 139
Kirkpatrick, A., Pope, A., Charmandaris, V., et al. 2013, ApJ, 763, 123
Kirkpatrick, A., Pope, A., Sajina, A., et al. 2015, ApJ, 814, 9
Lacy, M., Storrie-Lombardi, L. J., Sajina, A., et al. 2004, ApJS, 154, 166
Laigle, C., McCracken, H. J., Ilbert, O., et al. 2016, ApJS, 224, 24
Le Floc'h, E., Aussel, H., Ilbert, O., et al. 2009, ApJ, 703, 222
Lee, J. C., Hwang, H. S., Lee, M. G., Kim, M., & Lee, J. H. 2012, ApJ, 756, 95
Leipski, C., Haas, M., Willner, S. P., et al. 2010, ApJ, 717, 766
Lutz, D., Poglitsch, A., Altieri, B., et al. 2011, A&A, 532, A90
Lyu, J., & Rieke, G. H. 2017, ApJ, 841, 76
Lyu, J., Rieke, G. H., & Alberts, S. 2016, ApJ, 816, 85
Ma, X., Hopkins, P. F., Faucher-Giguère, C.-A., et al. 2016, MNRAS, 456, 2140
Madau, P., & Dickinson, M. 2014, ARA&A, 52, 415
Marconi, A., & Hunt, L. K. 2003, ApJL, 589, L21
Mendez, A. J., Coil, A. L., Aird, J., et al. 2013, ApJ, 770, 40
Messias, H., Afonso, J., Salvato, M., Mobasher, B., & Hopkins, A. M. 2012, ApJ, 754, 120
Mullaney, J. R., Alexander, D. M., Aird , J., et al. 2015, MNRAS, 453, 83
Mullaney, J. R., Alexander, D. M., Goulding, A. D., & Hickox, R. C. 2011, MNRAS, 414, 1082
Mullaney, J. R., Pannella, M., Daddi, E., et al. 2012, MNRAS, 419, 95
Murphy, E. J., Chary, R.-R., Dickinson, M., et al. 2011, ApJ, 732, 126
Oliver, S. J., Bock, J., Altieri, B., et al. 2012, MNRAS, 424, 1614
Pandya, V., Brennan, R., Somerville, R. S., et al. MNRAS, 472, 2054
Pannella, M., Elbaz, D., Daddi, E., et al. 2015, ApJ, 807, 141

Papovich, C., Dole, H., Egami, E., et al. 2004, ApJS, 154, 70
Papovich, C., Rudnick, G., Rigby, J. R., et al. 2009, ApJ, 704, 1506
Peeters, E., Spoon, H. W. W., & Tielens, A. G. G. M. 2004, ApJ, 613, 986
Pérez-González, P. G., Egami, E., Rex, M., et al. 2010, A&A, 518, L15
Pérez-González, P. G., Rieke, G. H., Egami, E., et al. 2005, ApJ, 630, 82
Petric, A. O., Armus, L., Howell, J., et al. 2011, ApJ, 730, 28
Pope, A., Chary, R.-R., Alexander, D. M., et al. 2008, ApJ, 675, 1171
Rawle, T. D., Altieri, B., Egami, E., et al. 2016, MNRAS, 459, 1626
Rieke, G. H., Alonso-Herrero, A., Weiner, B. J., et al. 2009, ApJ, 692, 556
Rigby, J. R., Marcillac, D., Egami, E., et al. 2008, ApJ, 675, 262
Rosario, D. J., Santini, P., Lutz, D., et al. 2013, ApJ, 771, 63
Rujopakarn, W., Dunlop, J. S., Rieke, G. H., et al. 2016, ApJ, 833, 12
Rujopakarn, W., Rieke, G. H., Eisenstein, D. J., & Juneau, S. 2011, ApJ, 726, 93
Sajina, A., Spoon, H, Yan, L., et al. 2009, ApJ, 703, 270
Sajina, A., Yan, L., Fadda, D., et al. 2012, ApJ, 757, 13
Sanders, D. B., Salvato, M., Aussel, H., et al. 2007, ApJS, 172, 86
Sanders, D. B., Soifer, B. T., Elias, J. H., et al. 1998, ApJ, 325, 74
Sanders, R. L., Shapley, A. E., Kriek, M., et al. 2015, ApJ, 799, 138
Sandstrom, K. M., Bolatto, A. D., Bot, C., et al. 2012, ApJ, 744, 20
Santini, P., Ferguson, H. C., Fontana, A., et al. 2015, ApJ, 801, 97
Scoville, N. 2007, AIPC, 943, 221
Shipley, H. V., Papovich, C., Rieke, G. H., et al. 2016, ApJ, 818, 60
Shivaei, I., Reddy, N. A., Shapley, A. E., et al. 2017, ApJ, 837, 157
Siebenmorgen, R., Heymann, F., & Efstathiou, A. 2015, A&A, 583, 120
Smith, J. D. T., Draine, B. T., Dale, D. A., et al. 2007, ApJ, 656, 770
Spoon, H. W. W., Marshall, J. A., Houck, J. R., et al. 2007, ApJL, 654, L49
Stanley, F., Harrison, C. M., Alexander, D. M., et al. 2015, MNRAS, 453, 591
Stefanon, M., Haojing, Y., Mobasher, B., et al. 2017, ApJS, 229, 32
Steffen, A. T., Strateva, I., Brandt, W. N., et al. 2006, AJ, 131, 2826
Stern, D., Eisenhardt, P., Gorjian, V., et al. 2005, ApJ, 631, 163
Sun, M., Trump, J. R., Brandt, W. N., et al. 2015, ApJ, 802, 14
Teng, S. H., Rigby, J. R., Stern, D., et al. 2015, ApJ, 814, 56
Vasudevan, R. V., & Fabian, A. C. 2007, MNRAS, 381, 1235
Veilleux, S., Rupke, D. S. N., Kim, D.-C., et al. 2009, ApJS, 182, 628
Vignali, C., Brandt, W. N., & Schneider, D. P. 2003, AJ, 125, 433
Wells, Pel, J.-W., Glasse, A., et al. 2015, PASP, 127, 646
Xue, Y. Q., Luo, B., Brandt, W. N., et al. 2011, ApJS, 195, 10
Younger, J. D., Fazio, G. G., Huang, J.-S., et al. 2009, ApJ, 704, 803
Zahid, H. J., Geller, M. J., Kewley, L. J., et al. 2013, ApJL, 771, L19